

# INTERIM REPORT

Exploiting Electric and Magnetic Fields for Underwater  
Characterization

SERDP Project MR-1714

March 2011

Dr. Gregory Schultz  
Sky Research, Inc

*This document has been cleared for public release*



# Report Documentation Page

Form Approved  
OMB No. 0704-0188

Public reporting burden for the collection of information is estimated to average 1 hour per response, including the time for reviewing instructions, searching existing data sources, gathering and maintaining the data needed, and completing and reviewing the collection of information. Send comments regarding this burden estimate or any other aspect of this collection of information, including suggestions for reducing this burden, to Washington Headquarters Services, Directorate for Information Operations and Reports, 1215 Jefferson Davis Highway, Suite 1204, Arlington VA 22202-4302. Respondents should be aware that notwithstanding any other provision of law, no person shall be subject to a penalty for failing to comply with a collection of information if it does not display a currently valid OMB control number.

1. REPORT DATE <b>MAR 2011</b>		2. REPORT TYPE		3. DATES COVERED <b>00-00-2011 to 00-00-2011</b>	
4. TITLE AND SUBTITLE <b>Exploiting Electric and Magnetic Fields for Underwater Characterization</b>				5a. CONTRACT NUMBER	
				5b. GRANT NUMBER	
				5c. PROGRAM ELEMENT NUMBER	
6. AUTHOR(S)				5d. PROJECT NUMBER	
				5e. TASK NUMBER	
				5f. WORK UNIT NUMBER	
7. PERFORMING ORGANIZATION NAME(S) AND ADDRESS(ES) <b>Sky Research, Inc,445 Dead Indian Memorial Road,Ashland,OR,97520</b>				8. PERFORMING ORGANIZATION REPORT NUMBER	
9. SPONSORING/MONITORING AGENCY NAME(S) AND ADDRESS(ES)				10. SPONSOR/MONITOR'S ACRONYM(S)	
				11. SPONSOR/MONITOR'S REPORT NUMBER(S)	
12. DISTRIBUTION/AVAILABILITY STATEMENT <b>Approved for public release; distribution unlimited</b>					
13. SUPPLEMENTARY NOTES					
14. ABSTRACT					
15. SUBJECT TERMS					
16. SECURITY CLASSIFICATION OF:			17. LIMITATION OF ABSTRACT	18. NUMBER OF PAGES	19a. NAME OF RESPONSIBLE PERSON
a. REPORT <b>unclassified</b>	b. ABSTRACT <b>unclassified</b>	c. THIS PAGE <b>unclassified</b>			

This report was prepared under contract to the Department of Defense Strategic Environmental Research and Development Program (SERDP). The publication of this report does not indicate endorsement by the Department of Defense, nor should the contents be construed as reflecting the official policy or position of the Department of Defense. Reference herein to any specific commercial product, process, or service by trade name, trademark, manufacturer, or otherwise, does not necessarily constitute or imply its endorsement, recommendation, or favoring by the Department of Defense.

## EXECUTIVE SUMMARY

This project was undertaken by Sky Research Inc. (SKY) and the Woods Hole Oceanographic Institute (WHOI) to investigate the overall potential for electric (E) and magnetic (B) field sources and sensors to exploit the physics of the underwater environment. The ultimate goal of this project is to determine the E and B field designs that are best suited for underwater ordnance (UWO) applications. This interim report documents the results for the first year of work and recommendations for the second year. Based on the results from modeling and experimental efforts, further work is clearly warranted to develop and validate a working prototype system employing the components tested and applying the principles developed during our Year 1 study.

### Summary of Work To-Date

In Year 1, we set out to provide a basis for potential design strategies for E and/or B field sensing with the goal of detecting scattered target fields at 1-4 meter standoff over the frequency range of 100 Hz to 1 MHz. This basis was provided through modeling and simulation, preliminary experiments, and assessments of commercially available marine sources and sensors. To summarize the first year's results:

- Analytical E and B field models were developed, validated, and applied to understand the expected signals generated from marine environments at the scales relevant to the UWO problem. New numerical models based on the 3-dimensional Method of Auxiliary Sources were also developed and validated to simulate E and B field components generated by electric field sources such as insulated and bare dipole electrode configurations.
- Model results from the application of analytical and numerical representations of submerged transmitter sources provided an understanding of the interplay between inductively coupled conduction currents and electrical charges present in conductive media such as saltwater. The balance of energy between E and B field components of source fields was shown to be strongly frequency dependent. We found a strong influence from the E field unlike our experience in terrestrial electromagnetics where only the B field has significant influence.
- The attenuation of source fields was accurately accounted for in both analytical and numerical models in order to quantify the practical limits on standoff excitation for induction coil (magnetic dipole) and electrode (electric dipole) transmitters. Our results show that both sources generate sufficient fields to excite targets at ranges of 1-4 meters given sufficient power and geometrical considerations are followed. Of particular importance, was the finding that the magnetic field from the galvanically coupled electric dipole source (conduction currents) was particularly strong and tended to fall off at a slower rate than the induced magnetic field from a magnetic dipole source ( $1/r^2$  compared to  $1/r^3$ ).
- Development and engineering analysis of experimental marine-grade electrical dipole and magnetic induction loop transmitters enabled preliminary data collection and experimentation with a great deal of configurability. Combining our custom transmitters with commercially available electric (Ag/AgCl electrodes) and magnetic (wideband induction coil B-field sensors) receivers formed an initial testbed for lab and open water experiments.
- Open water experiments using the E and B field transmitters provided validation for the simulated field values at distances between 2 and 7.5 meters. High signal-to-noise ratios

(SNR) were observed in magnetic fields generated from both magnetic and electric dipole sources out to 7 meters from the source. High SNR values were maintained in the scattered field response produced by a target in the vicinity of the source excitation field. At a range of 1 meter from the receiver, we measured scattered magnetic fields produced by a UXO simulant that yielded SNR values of 45 dB and 43 dB for excitation from an electric dipole source and a magnetic dipole source, respectively. The magnetic field from a galvanically coupled electric dipole source at distance exceeded that from the magnetic dipole due to improved attenuation characteristics with range. This is a significant finding that may lead to improved performance using an electric field source rather than marine versions of terrestrial induction coil sources (e.g., EM-61S).

- Interaction with the seafloor and sea surface interfaces was introduced to our models and the effects of varying seafloor conductivity for different source types (electric or magnetic, frequency, configuration) were compared. The surface interaction component, which is typically utilized for large scale (over kilometers) marine electromagnetic work (e.g., hydrocarbon and sediment mapping) was also found to influence E and B field signals within 10 meters of the source, but only at frequencies >50 kHz.
- Application of modeling methods to canonical metallic targets revealed the increased influence of the scattered electric field with frequency relative to the magnetic field. The relative strength of the scattered electric field can also be related to the conductivity of water column and coincides with the direct current field behavior. We observe detectable ( $>\mu\text{Am}^2$ ) scattered magnetic fields for simulated steel objects excited with an electric dipole source at offsets over 1 meter from the target.
- The theoretical differences between the induced fields (derived from currents) versus those that are galvanically coupled (derived from charges) for targets excited underwater support the potential of electric field excitation and/or sensing. We also found that offsetting transmitters and receivers (non-coincident) leads to larger signals due to the balance between scattered and primary electric and magnetic fields. We believe this will be an important design consideration for future optimized systems.
- Raw secondary magnetic field signals from simulant UXO objects placed 40-60 cm from a wideband induction coil B-field receiver decayed from a few nT to zero over 3 to 20 ms. The form of decay curves were influenced by target orientation and material type (ferrous versus non-ferrous) regardless of the source used.
- While some preliminary investigations using electric field sensors showed potential for characterizing the induced polarization (at <1 kHz) and scattering (at >10 kHz), the full potential of these sensors was not realized in these experiments. Our modeling results do indicate that at relatively low frequencies or short ranges, the galvanically coupled electric field can be caused by both conductive and resistive inhomogeneities. The practical implication (although not validated with field data) is that contrasts in resistivity of the seafloor may manifest as noise in E-field sensors.

## Findings and Recommendations

In the first year of this project we set out to determine:

1. If E and B field sources could generate adequate electromagnetic excitation of targets at standoff distances between 1-4 m.
2. If there was promise in exploiting E and B fields at frequencies >10 kHz where distortion (relative to in-air case) of signals occurs.

3. If commercial marinized E and B field sensors existed that could exploit the higher frequencies of interest at suitable SNR values.

We have shown through a combination of modeling and experimental data analysis that the concept of tailored E- and B-field sensing designs can lead to improved performance over marinization of terrestrial EM systems. We found and tested a number of commercially available wideband sensors that maintain excellent sensitivity at the higher frequencies of interest. Through a number of model scenarios we learned that at frequencies  $>20$  kHz an induction coil (magnetic dipole) transmitter imparts electric field intensities comparable to the magnetic field and should be accounted for in models of target or seafloor interaction. Experimental studies revealed that the electric dipole (generated by a non-polarizing graphite electrode) primarily generates electric field signals that are proportional to the potential difference across the electrodes, as predicted by analytical and numerical models. Additionally, E-field source experiments produced measurements of relatively strong magnetic fields at a distance  $>2$  m from the transmitter. Because galvanic coupling from an electric dipole source was found to generate strong and widely distributed primary field conduction currents that fall off as  $1/r^2$ , we think that a carefully designed E-field transmitter will generate adequate excitation of targets at standoff distances up to 3 meters. Coupled with potential for improved form factor and reduced hydrodynamic drag, we contend that this source may ultimately outperform an induction coil transmitter as a source when cost effectiveness, ease of deployment, and source strength at range are considered.

Further work is warranted to develop and test a system design. A summary of the tasks we will undertake in Year 2 is as follows:

- Apply models developed in Year 1 to investigate optimized source/receiver configuration design. Extend analysis of model results to better understand the balance of galvanically and inductively coupled EM fields into the seafloor and onto target objects. Analyze target localization and parameterization using sensitivity analyses.
- Develop and trial an electric dipole source based on lessons learned from our previous experimental system. Extend and test a configurable source input design that enables wideband excitation fields with the goal of achieving 200 kHz bandwidth.
- Conduct testing of the B and E field receiver configurations to determine optimal deployment strategies. Testing will include full parameterization of a selected B-field receiver (via the configurable wideband transmitter) as well as investigation of the feasibility of deploying E-field receivers in addition to the wideband B receiver.
- Configure and test a prototype system deployed from a tow vessel. We will leverage our existing SKY and/or WHOI vessels, tow assemblies, instrument validation and testing installations, and associated navigation and positioning assets to maximize field testing effectiveness. Data collection and analysis will focus on range sensitivity, SNR metrics, and target characterization, as well as the advantages and limitations of various deployment strategies.

## TABLE OF CONTENTS

<b>Executive Summary</b> .....	<b>1</b>
<b>Table of Contents</b> .....	<b>4</b>
<b>1. Project Background and Objectives</b> .....	<b>5</b>
<b>1.1. Motivation and Technology Leveraging Opportunity</b> .....	<b>5</b>
<b>1.2. Objectives</b> .....	<b>6</b>
<b>2. Summary of Year 1 Results</b> .....	<b>6</b>
<b>2.1. Task 1 – Modeling and Simulation</b> .....	<b>6</b>
<b>2.1.1. Submerged E and B Field Transmitter Sources</b> .....	<b>8</b>
<b>2.1.2. Seafloor Interaction</b> .....	<b>16</b>
<b>2.1.3. Target Scattering</b> .....	<b>22</b>
<b>2.2. Task 2 – Controlled Data Collection and Experimentation</b> .....	<b>27</b>
<b>2.2.1. Electric Field Laboratory Data Collection</b> .....	<b>28</b>
<b>2.2.2. Open Water Experiments</b> .....	<b>31</b>
<b>2.3. Task 3 – Sensor Assessment and Concept Design Feasibility</b> .....	<b>36</b>
<b>2.3.1. Source Concepts</b> .....	<b>36</b>
<b>2.3.2. Source Design</b> .....	<b>39</b>
<b>2.3.3. Receiver Concepts</b> .....	<b>41</b>
<b>2.3.4. Receiver Design</b> .....	<b>43</b>
<b>3. Year 2 Suggested Work</b> .....	<b>44</b>
<b>References</b> .....	<b>46</b>

## **1. Project Background and Objectives.**

Under SERDP project MR-1714, Sky Research and the Woods Hole Oceanographic Institute investigated the application of marine magnetic and electric field sensing techniques for detecting and characterization underwater ordnance (UWO). Our approach has been founded on the basis that the electromagnetic properties of underwater environment will enable an extension of the useful magnetic sensing methods employed in terrestrial applications. This report summarizes the results from the first year of this project and presents a suggested plan for continued work in 2011 and 2012. For brevity, only select results are described in detail with emphasis on those results that guide the decision to proceed with continued work in a second year.

### **1.1. Motivation and Technology Leveraging Opportunity.**

Current underwater geophysical surveys are primarily limited to passive magnetic systems towed from a surface vessel. These systems utilize fluxgate, Overhauser, or atomic magnetometer sensors, often deployed in arrays towed from the stern of small to moderate-size vessels. Active source electromagnetic methods have been utilized to a lesser extent. These systems generally consist of pulsed induction or swept frequency induction coil transmitter and receiver pairs or arrays. A few commercialized systems, mostly based on terrestrial EM systems, have been developed and deployed. While ground-based sensing methodologies have experienced some limited success when applied to the underwater environment, the fundamental electromagnetic characteristics of marine media require an alteration of terrestrial paradigm to fully exploit these conventional methodologies. Specifically, there is much evidence that employing electromagnetic modes that are higher in frequency than those typically used in ground-based sensing will yield greater range and sensitivity for underwater surveys.

Conventional electromagnetic sensing for UXO on land utilizes only magnetic sources and receivers (induction coils). By contrast, underwater/marine geophysics can utilize both electric and magnetic sensors. Four fundamental source types exist: vertical and horizontal magnetic dipoles (VMD and HMD; i.e., loop current source) and vertical and horizontal electric dipoles (VED and HED; i.e., dipole sources). Varying configurations of electric field sensors have been attempted during research and development activities. These include adaptation of ground penetrating radar methods for freshwater UXO detection (SERDP MM-1441), implementation of marine direct-current or streaming resistivity methods, and experimentation with induced polarization (SERDP MM-1325) and electric field sensing. However, electric field sensors have not been used in operational UXO surveys in North America to the best of our knowledge.

Magnetic dipoles consist of closed loops of insulated, current-carrying wire and electric dipoles are generally in the form of insulated, current-carrying wire with bare ends (or potted electrodes). In the surrounding media, each source type generates some combination of transverse magnetic (toroidal mode, TM) or transverse electric (poloidal mode, TE) propagation modes relative to the seafloor:

- Vertical magnetic dipole (VMD) – induces only TE modes
- Horizontal magnetic dipole (HMD) – induces both TM and TE modes
- Vertical electrical dipole (VED) – induces only TM modes
- Horizontal electric dipole (HED) – induces both TM and TE modes

In marine applications, the source is embedded in the conductive medium rather than lying on a

conductive half-space. Therefore, preconceptions based on terrestrial applications can be non-intuitive and quite misleading. For instance, HED and HMD systems produce and receive both TM and TE modes in the sea (unlike on the surface of the Earth). The marine VMD system, as in its terrestrial analog, is only dependent on TE mode propagation; however, the secondary fields from this source are measured near the surface of the strongly conducting saltwater medium. In this case, the component of the secondary field we are trying to measure will largely vanish at the surface due to the strong conductivity contrast and will not be as sensitive to targets buried in seafloor sediments as the HED or HMD configurations (Figure 1).

**1.2. Objectives.**

The main motivation for this project was the potential to exploit both magnetic and electric field information for detection, localization, and discrimination of underwater UXO. Our approach is to leverage existing underwater electromagnetic methods that utilize electric and magnetic fields. The objectives for this project are to:

1. Develop potential design strategies for implementing both magnetic and electric field sensors in the marine environment, and we will determine the best arrangement for a potential combined electric and magnetic field sensing system with the goal of sensing fields at 1-4 m standoff within the frequency range 100 Hz to 1 MHz.
2. Evaluate the information content in VLF/LF (10 kHz to 1 MHz) range to exploit both magnetic and electric field information for detection, localization, and discrimination of UXO. Establish the applicability of electric field sensing for UWO detection.
3. Determine the electric and magnetic field sensing designs that are best suited for UWO applications. Build and test a prototype electric and magnetic field sensing system and generate first-order results that explore the utility of this methodology to enhance existing EMI designs in UWO applications.

**2. Summary of Year 1 Results.**

Through modeling and simulation combined with experimental data collection and analyses, we found that underwater electromagnetic UXO technology can be tailored to detect and characterize submerged UXO. Our research work also provided us with a thorough understanding of the physical interaction of both electric and magnetic fields with compact metallic targets and the seafloor. Our results suggest that electric field transmitters generate sufficient source field strengths at distances between 1 and 4 meters.

**2.1. Task 1 - Modeling and Simulation**

Using our existing algorithms and models developed under SERDP UX-1632 and other related

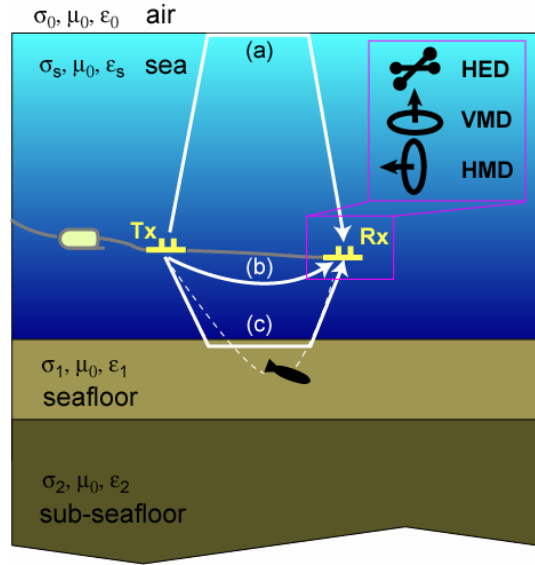


Figure 1. In marine applications, the source is embedded in the conductive medium rather than lying on a conductive half-space. Under these conditions, HED and HMD systems produce and receive both TM and TE modes in the sea (unlike on the surface of the Earth). Total fields represent the superposition of direct, reflected, and interaction with sea surface and seafloor interfaces.

work, we assessed the veracity of E- and B-field responses in the VLF/LF frequency range. In this Task, we utilized these models and others developed by the team to predict the potential applicability of VLF/LF field sensing.

Solutions for both electric and magnetic field characterization are well-established in layered terrestrial media. Numerical and analytical models for sources in conductive media have also been developed, but are often validated at much larger scales than those of interest in this study. For example, a number of 1, 2, and 3-D models have been developed for petroleum exploration using controlled-source EM methods. These models are often only appropriate at large offset ranges or in very deep water. Chave and Cox [1982] have developed exact closed-form solutions for vertical and horizontal electrical dipole sources that are appropriate at any range or depth. In addition, Chave [2009] has compiled a complete set (all combinations of dipole configurations) of closed-form solutions for both magnetic and electric sources in conductive media. We utilize this formulation for understanding the propagation of magnetic and electric fields near the seafloor. These solutions present models for the various electric and magnetic sources in terms of complex Hankel transforms (integrals of kernel functions multiplied by Bessel functions of the appropriate Green's function expressions). These integrals are solved by approximation or asymptotic solutions and can also be integrated numerically.

Maxwell's equations for an isotropic medium of conductivity  $\sigma$ , permeability  $\mu$ , and dielectric permittivity  $\epsilon$ :

$$\nabla \times \mathbf{H} = (\sigma + i\omega\epsilon)\mathbf{E} + \mathbf{J} \quad \text{and} \quad (1)$$

$$\nabla \times \mathbf{E} = i\omega\mu\mathbf{H}, \quad (2)$$

with the electric  $\mathbf{E}$  and magnetic  $\mathbf{B}$  fields can be represented by the magnetic vector potential  $\mathbf{A}$ , with propagation constant  $k$

$$\mathbf{E} = \frac{i\omega}{k^2} \nabla \nabla \cdot \mathbf{A} - i\omega\mathbf{A} \quad \text{and} \quad (3)$$

$$\mathbf{B} = \mu\mathbf{H} = \nabla \times \mathbf{A}, \quad (4)$$

where  $k^2 = i\omega\mu\sigma - \omega^2\mu\epsilon$ . The vector potential and associated electric and magnetic fields can be found by solving the Helmholtz equation  $\nabla^2 \mathbf{A} - k^2 \mathbf{A} = \mu\mathbf{J}$ .

We use both numerical and analytical techniques to simulate the propagation from various source types and scattering of both magnetic and electric field components. Analytical and semi-analytical methods assume isotropic one-dimensional media and represent scattering objects by dipole approximations. These solutions are obtained through the use of complex image theory or asymptotic approximation to the wavenumber domain integral equations. Our numerical approach utilizes the *Method of Auxiliary Sources* (MAS) to represent both sources and scattering objects in three dimensions (Shubiditze, 2009). The boundary value problems are solved for EM fields in each domain by finite linear combination of sources placed along the surfaces of structures or objects. The tangential components of the electric and magnetic fields are continuous across each boundary:

$$(\mathbf{E}_2 - \mathbf{E}_1) \times \hat{\mathbf{n}} = 0, \quad \text{and} \quad (5)$$

$$(\mathbf{H}_2 - \mathbf{H}_1) \times \hat{\mathbf{n}} = 0. \quad (6)$$

In some cases, approximate solutions are advantageous when computation time and complexity

precludes a thorough investigation of particular effects. In such situations, we will utilize one-dimensional models such as those derived from the theory of complex images (e.g., Bannister, 1984) and from approximations of infinite integrals (e.g., Loseth, 2007). These formulations are not exact, but provide very efficient and accurate solutions for many scenarios. For example, Bannister [1984] extended his complex image theory models for sources and receivers in conductive media for the magnetic and electric dipole configurations of interest here. The formulas are completely general and valid at any frequency range for a flat seafloor double half-space model configuration.

### 2.1.1. Submerged E- and B-field Transmitter Sources

Simulations of active magnetic and electric field sources have been developed and utilized. We first consider electric and magnetic field sources located in a conductive seawater whole space. This simplifies the solution with regard to interaction at interfaces and allows us to simulate the baseline source field for which we will compare to more complex models that incorporate seafloor or sea surface as well as experimental data.

Wait [1952] has considered the insulated magnetic dipole in a conducting medium, where it was shown that the source fields from the dipole are not dependent on the characteristics of the insulation if the overall diameter of the induction coil antenna is much less than the effective wavelength in the conducting medium. Since the smallest wavelength we consider for nominal seawater (4 S/m) is on the order of 2-5 meters (corresponding to 1 MHz and 100 kHz), it will be assumed that this condition is satisfied. An induction loop transmitter is represented as a magnetic dipole of strength  $i\mu\omega\frac{IdA}{4\pi}$ , where  $I$  is the current in loop of area  $dA$ . It was found that this configuration in seawater will give rise to TE spherical waves both inside (in air) and outside (in the seawater) the insulated cavity where the induction coil resides. Choosing a polar coordinate system and formulating Maxwell's equations in terms of the scalar wave function  $\psi$  we have:

$$r^2 \frac{\partial^2 \psi}{\partial r^2} + \frac{1}{\sin \theta} \frac{\partial}{\partial \theta} \left( \sin \theta \frac{\partial \psi}{\partial \theta} \right) - k^2 r^2 \psi = 0. \quad (7)$$

Solutions can be formed by applying the boundary conditions, which require the continuity of the tangential electric and magnetic fields across the insulator-sea boundary:

$$H_r = \frac{M(a) \cos \theta}{2\pi r^3} (1 + kr) e^{-kr} \quad (8a)$$

$$H_\theta = \frac{M(a) \sin \theta}{4\pi r^3} (1 + kr + k^2 r^2) e^{-kr}, \text{ and} \quad (8b)$$

$$E_\phi = \frac{-i\omega\mu M(a) \sin \theta}{4\pi r^2} (1 + kr) e^{-kr}, \quad (8c)$$

where  $M(a) = IdA \frac{3e^{ak}}{(3 + 3ak + a^2 k^2)}$  is the equivalent magnetic dipole contained within the insulating cavity of radius  $a$ . At any point in space the total time-varying magnetic field will be the vector sum of  $H_\theta$  and  $H_r$ . If we take  $\theta = 90^\circ$ , i.e. the point of measurement in the plane of the loop, then  $H_\theta \rightarrow 1$  and  $H_r \rightarrow 0$ . The near field attenuation from the dipole reveal sthe expected  $1/r^3$  fall off for the magnetic field and  $1/r^2$  fall off for the electric field. Wait [1951] approximates the total power  $P$  crossing the wall of the cavity from half of the real part of the radial component

of the Poynting vector as  $P \approx (IdA)^2 \frac{\sigma(\omega\mu)^2}{12\pi a}$ .

Examples of applying these analytical formulations for a magnetic field source (induction coil) are shown in Figure 2. Here we simulate the distribution of electromagnetic energy in water with conductivity of 4 S/m. A 20 cm radius insulated cylindrical coil is assumed for the magnetic dipole source. The near field distributions for the vertical and radial components of the magnetic reveal significant attenuation regardless of frequency. The tangential electric field component, on the other hand, is highly dependent on frequency, where source fields scale with frequency. At the lower frequency of 5 kHz the magnetic field dominates the area around the source. However, at 50 kHz the electric and magnetic field components are nearly equivalent in amplitude (in their respective engineering units, Am and V/m).

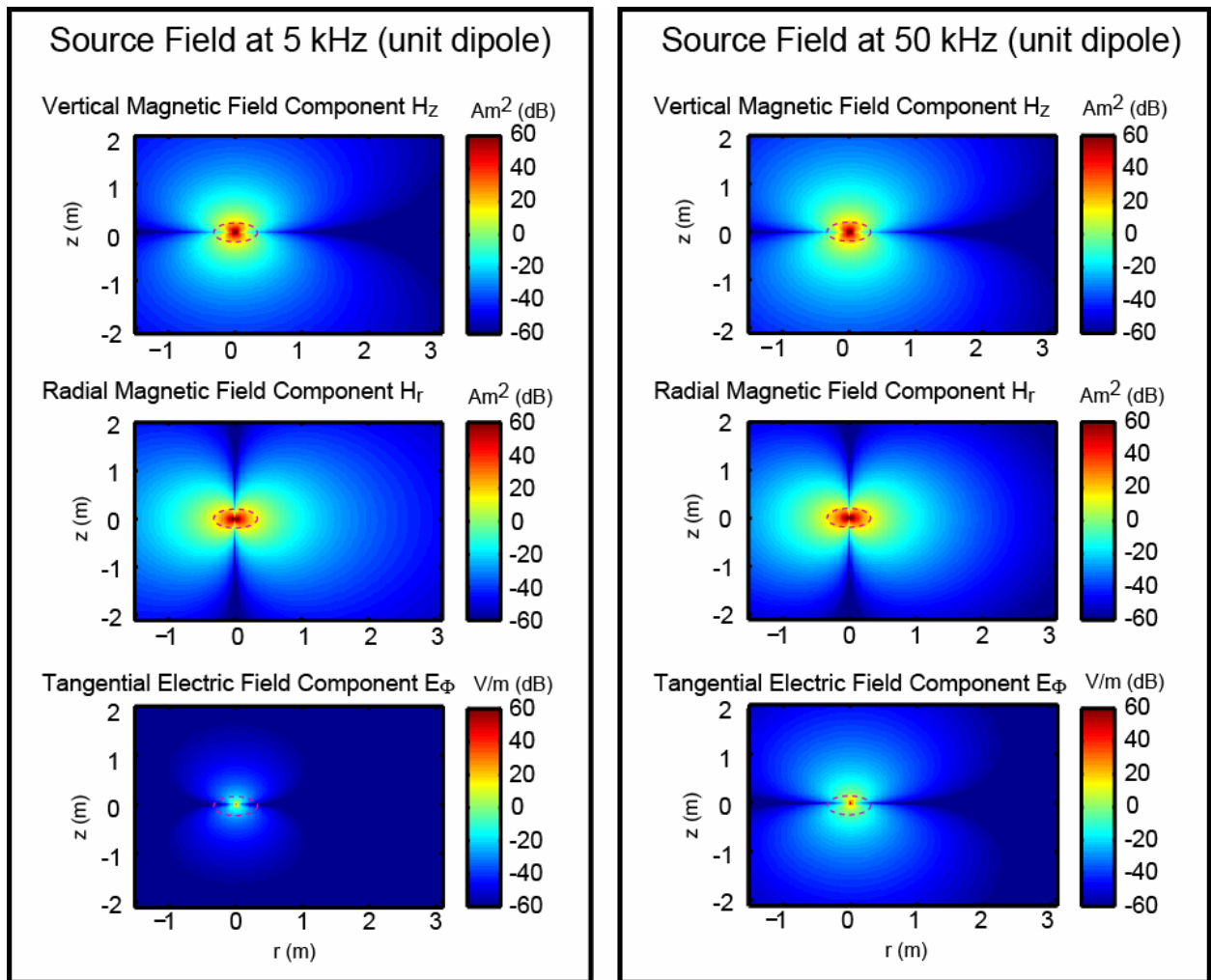


Figure 2. Examples of the application of analytical formulations at 5 and 50 kHz for a VMD source. At the lower frequency of 5 kHz the electric field is not very strong relative to the magnetic field. At 50 kHz the tangential component of the electric field has increased significantly in relation to the magnetic field strength.

Similar analytical formulations exist for an electric field source submerged in a infinite conductive

medium. We derive both the electric and magnetic field components from Maxwells equations, e.g.,  $\nabla \times \mathbf{H} = (\sigma + i\omega\epsilon)\mathbf{E} + \mathbf{J} = i\omega\epsilon\mathbf{E} + \sigma\mathbf{E} + \mathbf{J}$ . In the first case we consider the source fields generated from the impressed current density  $\mathbf{J}$  and the induced current conduction term  $\sigma\mathbf{E}$ .

We utilize the formulation of Wait [1953] and Inan et al. [1985], which assume an isotropic, homogeneous, and time-invariant conducting medium and adequately thin, finite, insulated wire element cross-section. The geometry of the current element carrying  $Ie^{i\omega t}$  extends from  $l_1$  to  $l_2$  along the axial direction,  $x$ , in cylindrical coordinates. The electric and magnetic field components are:

$$E_\rho = \frac{rI}{4\pi\sigma} \left[ \frac{e^{-kr_2}}{r_2^3} (1 + kr_2) - \frac{e^{-kr_1}}{r_1^3} (1 + kr_1) \right] \quad (9a)$$

$$E_x = \frac{i\omega\mu I}{4\pi} \left[ \left( \sinh^{-1} \frac{x-l_2}{\rho} - \sinh^{-1} \frac{x-l_1}{\rho} - E_c(r, x_2) + E_c(r, x_1) \right) - i(E_s(r, x_2) - E_s(r, x_1)) \right] + \frac{I}{4\pi} \left[ \left( (x-l_2) \frac{e^{-kr_2}}{r_2^3} (1 + kr_2) - (x-l_1) \frac{e^{-kr_1}}{r_1^3} (1 + kr_1) \right) \right], \quad (9b)$$

and

$$H_\phi = \frac{(\sigma + i\omega\epsilon)}{k^2} \frac{\partial E_x}{\partial \rho} = -\frac{I}{4\pi} \frac{\partial}{\partial \rho} \int_{l_1}^{l_2} \frac{e^{-kr}}{r} dl, \quad (9c)$$

where  $E_c(r, x)$  and  $E_s(r, x)$  are the generalized cosine and sine integrals (Inan, et al., 1985).

Examples of the application of these analytical formulations are shown in Figures 3 for oscillating current at 5 and 50 kHz. The relatively complex distribution of the line current (electrode) source very near the electrode tends to approximate a dipole at greater distances from the source. As expected, our numerical results show evidence of exponential attenuation as the fields propagate in the conducting medium. The parallel component of the amplitude of the electric field  $E_x$  has the greater variation with change in frequency. The perpendicular component of the electric field  $E_r$  remains relatively constant over this frequency range, while the total magnetic field tends to attenuate at higher frequencies. At the lower frequency of 5 kHz the electric field components are not very strong relative to the magnetic field. At 50 kHz the parallel component of the electric field has increased significantly in relation to the magnetic field strength.

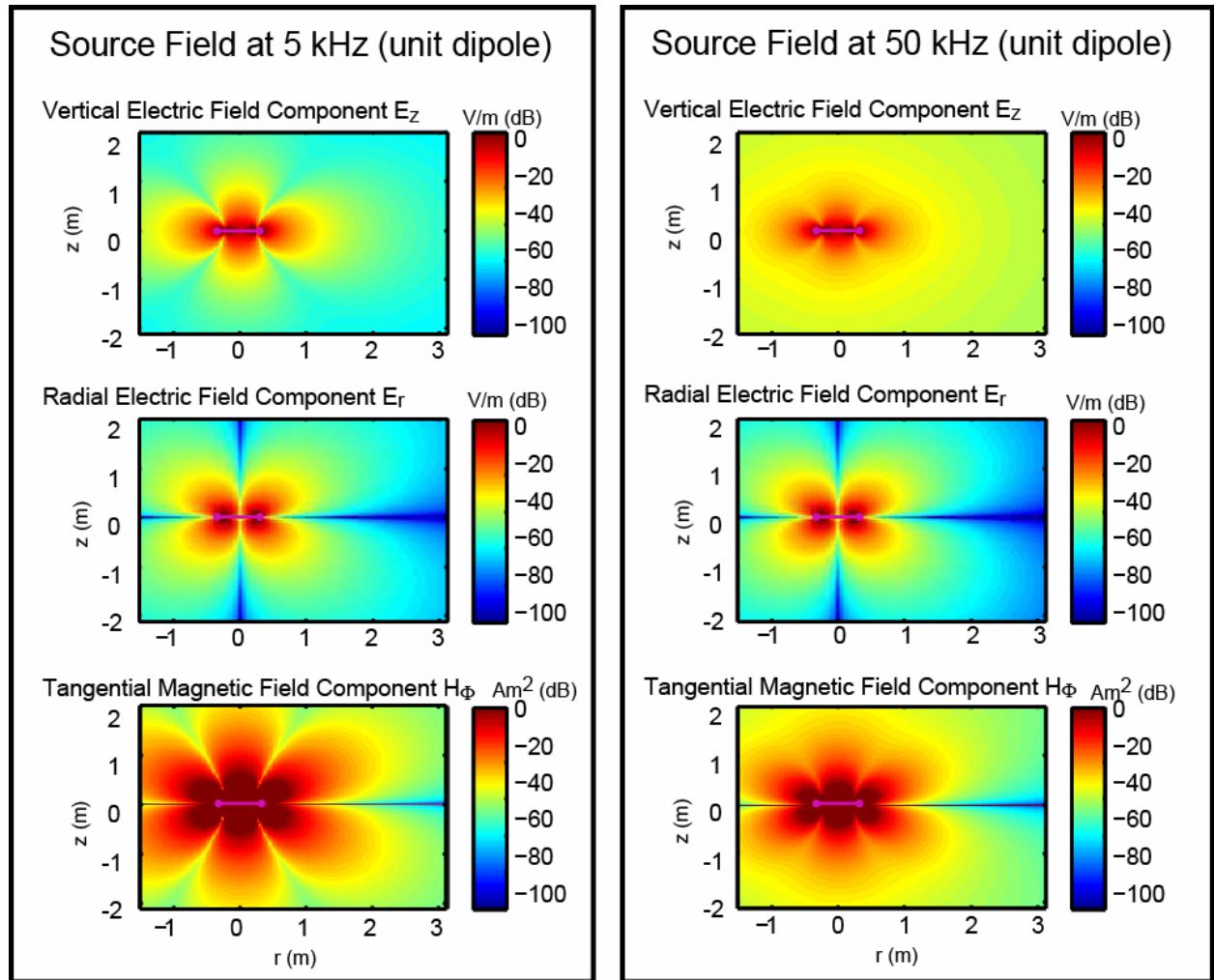


Figure 3. Examples of the application of analytical formulations at 5 and 50 kHz for a HED source. The relatively complex distribution of the line current (electrode) source very near the electrode tends to approximate a dipole at greater distances from the source.

Because of their importance in generating electric and magnetic fields at distance from the source, we focused in more detail on the generation of conduction currents from a current driven electrode source. Assuming low frequencies and suppressing the time variation of the field for the moment, we derived the analytical model for a static dipole in a conducting medium. The goal here is to investigate the propagation of electric and magnetic fields purely through galvanic coupling with the surrounding water.

If we separate out the component of induced current conduction from Ampere’s circuital law and consider only the static case, we have the equation for Ohm’s law in vector form for current flow in a conductive medium. This represents the current density  $\mathbf{J} = \sigma\mathbf{E} = -\sigma\nabla\phi$  as a function of the conductivity and electric field intensity and/or the electrical potential  $\phi$ . We start by placing charges along the surfaces of a cylindrical electrodes and computing the electric field via Columb’s Law  $\mathbf{E} = \frac{1}{4\pi\epsilon} \sum_{i=1}^N \frac{q_i}{R_i^3} \vec{R}_i$ . We can then integrate over a spherical volume to solve for the

vector potential:

$$\mathbf{A} = \frac{\mu}{4\pi} \int_{V'} \frac{\mathbf{J}}{R} dV' = \frac{\mu\sigma}{4\pi} \int_{V'} \frac{\mathbf{E}}{R} dV' \quad (10)$$

$$\mathbf{A} = \frac{\mu}{4\pi} \int_{V'} \frac{\mathbf{J}}{R_1} dV' = \frac{\mu\sigma}{4\pi} \int_{V'} \frac{p[(2 \cos \theta' \sin \theta' \sin \phi' + \sin \theta' \cos \theta' \sin \phi')\mathbf{a}_y + (2 \cos^2 \theta' - \sin^2 \theta')\mathbf{a}_z]}{4\pi\epsilon R^3 \sqrt{(-R' \sin \theta' \cos \phi')^2 + (R \sin \theta - R' \sin \theta' \sin \phi')^2 + (R \cos \theta - R' \cos \theta')^2}} R'^2 \sin \theta' dR' d\theta' d\phi'$$

The curl of the vector potential can be used to determine the rotational magnetic field associated with the conduction currents generated from the electrode-water coupling:

$$\mathbf{H} = \frac{1}{\mu} \nabla \times \mathbf{A} = \hat{\mathbf{a}}_\phi \frac{1}{\mu R} \left[ \mathbf{A}_\theta + R \frac{\partial \mathbf{A}_\theta}{\partial R} - \frac{\partial \mathbf{A}_R}{\partial \theta} \right]. \quad (11)$$

This formulation is summarized in graphical form in Figure 4.

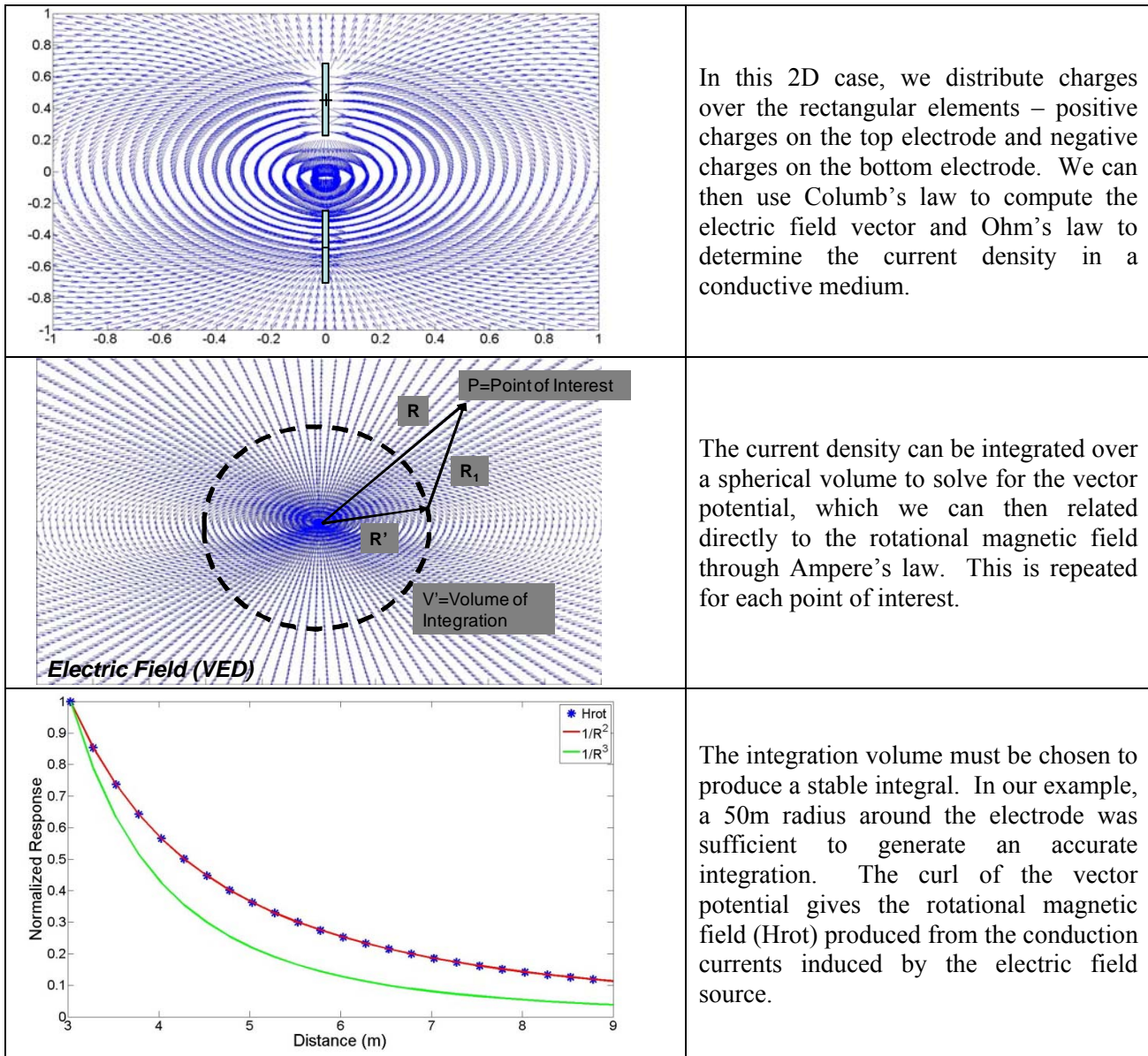


Figure 4. Overview of the numerical procedure used to simulate electrostatic galvanically coupled magnetic field distributions generated from a finite electrode transmitter.

Expanding  $R$  includes more volume current density. This is illustrated in Figure 5. Stability of integral is not achieved until we incorporate a relatively large volume around the electrodes.

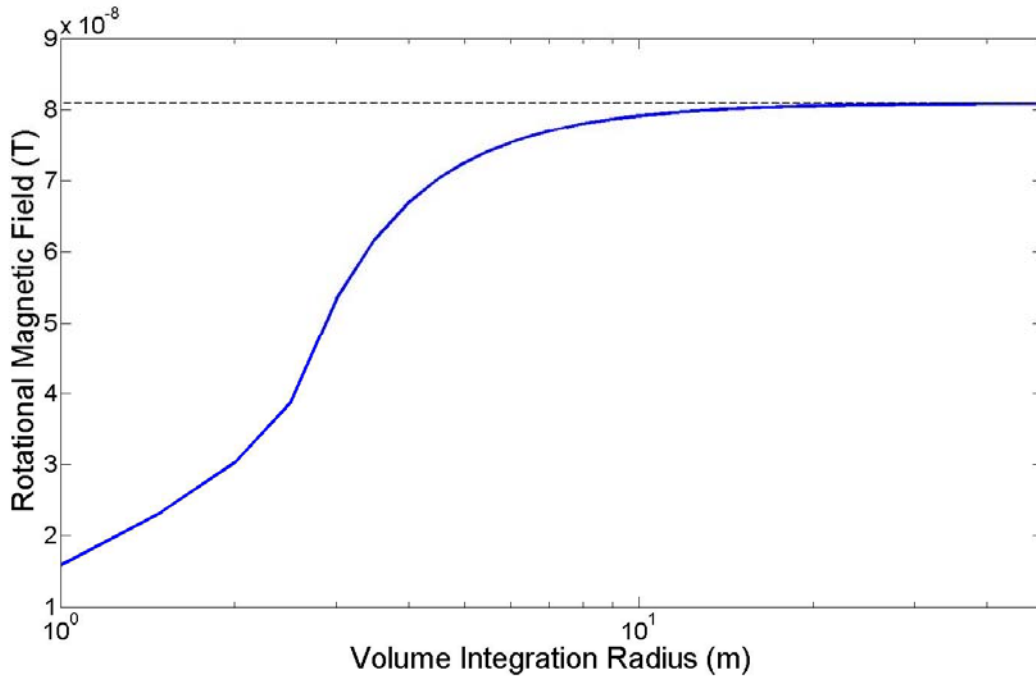


Figure 5. Effect of expanding the volume integration radius to achieve stable rotational magnetic fields generated by an electric dipole.

The current density produced from an electrostatic unit electric dipole source that is galvanically coupled to the seawater (4 S/m) generates a somewhat surprisingly large magnetic field. We attribute this to the strong conduction currents produced in conductive media such as saltwater. In addition, we found that relatively large volumes were required for integration of current density to produce the expected  $1/r^2$  behavior. This indicates that currents, although attenuated in strength, extend over large areas. We note that this is exactly the physical mechanism exploited for large scale controlled electromagnetic measurements that the marine geophysical exploration and production community has perfected for minerals and hydrocarbon applications. Here we show the potential to scale this method to smaller areas relevant to UXO detection and discrimination work.

To capture the full physical phenomenology of an electric field source in the underwater environment, we modified our MAS code for an electrode structure. The modified MAS uses electrical charges and currents as auxiliary sources. Application of this model permits simulation of arbitrarily shaped electric source transmitters embedded in conductive media or layered media. The basic structure of the model is shown in Figure 6.

The general principle of MAS is used in the formulation of the problem, by considering an auxiliary surface lying inside the wire antenna. However, since the diameter of the antenna is sufficiently small relative to the wavelength, the auxiliary sources used to model the electric source are distributed along an auxiliary line coinciding with the axis of the wire.

The auxiliary sources lying inside the wire dipole are used to describe the electromagnetic fields in transmitter's surrounding medium outside in the air region (1), as

$$\mathbf{E}(\mathbf{r}) = L^e[\mathbf{J}],$$

Where

$$L^e[\mathbf{J}] = j\omega\mathbf{A} - \nabla\varphi = \frac{j\omega\mu_0}{4\pi} \sum_{n=1}^{N_{dip}} \mathbf{J}_n G(\mathbf{r}, \mathbf{r}_n) - \frac{\nabla}{4\pi\epsilon_0} \sum_{n=1}^{N_{dip}} \rho_n G(\mathbf{r}, \mathbf{r}_n)$$

The charge density  $\rho$  on the dipole auxiliary line is related to the electric currents  $\mathbf{J}$  distributed on the same auxiliary line, by using the one-dimensional (1-D) finite difference approximation of the continuity equation.

$$\rho_n = \frac{1}{j\omega} \frac{J_{n+1/2} - J_{n-1/2}}{dz}$$

where  $G(\underline{r}, \underline{r}_n) = \exp(jkR_n)/R_n$  and  $k = k_0\sqrt{\epsilon}$  is the wave number inside the medium, with  $\epsilon$  being the relative complex permittivity of the dielectric medium. Similarly, the magnetic field produced by the electric source in transmitter surrounding medium can be written in terms of the defined auxiliary sources, as

$$\mathbf{H}(\mathbf{r}) = L^h[\mathbf{J}] = [\nabla \times \mathbf{A}] = \frac{\mu_0}{4\pi} \sum_{n=1}^{N_{dip}} \nabla \times [\mathbf{J}G(\mathbf{r}, \mathbf{r}_n)]$$

To determine the amplitudes of the induced  $\mathbf{J}$  current density, the boundary condition for the tangential electric field component vanishing on the metallic surface of the wire - with the exception of the feeding gap - are imposed at a finite number of (collocation) points  $\underline{r}_m = x_m\hat{x} + y_m\hat{y} + z_m\hat{z}$ , with  $-D/2 \leq z_m \leq D/2$ ,

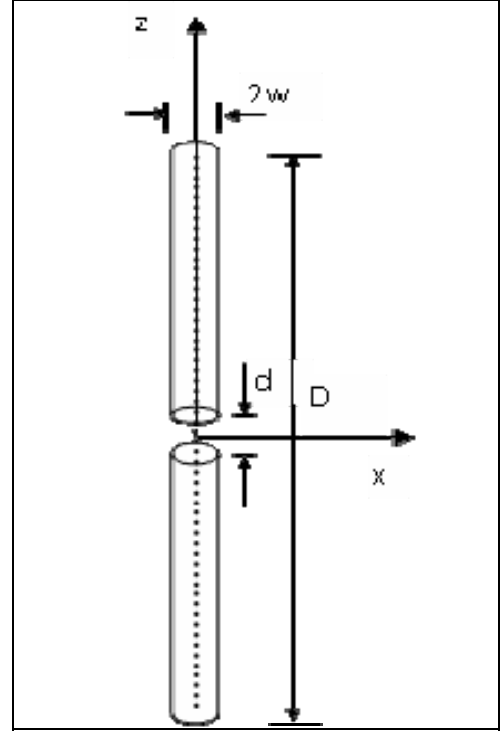


Figure 6. Representation of the electrode configuration used in the MAS model.

$$\hat{z} \cdot \underline{E}_1(\underline{r}_m) = \begin{cases} 0 & \text{if } \left| \frac{d}{2} \right| < |z_m| < \left| \frac{D}{2} \right| \\ \frac{V_0}{d} & \text{if } |z_m| \leq \left| \frac{d}{2} \right| \end{cases}, \quad m = 1, \dots, M_{dip}$$

where  $V_0$  is the voltage imposed at the feeding gap.

In addition the continuity condition at the wires beginning and ending points for the normal component of the current density  $\mathbf{J} = \sigma \mathbf{E} - j\omega \epsilon \mathbf{E} = \sigma_{eff} \mathbf{E}$ ,  $\sigma_{eff} = \sigma - j\omega \epsilon$  were enforced as:

$$\mathbf{J}_{1n} = \mathbf{J}_{2n}; \quad \sigma_{1,eff} \mathbf{E}_{1n} = \sigma_{2,eff} \mathbf{E}_{2n}.$$

The electric source is fed with an external voltage, which gives rise to electrostatic charge distributions on the electrodes. These static charges produce an electric field, which, in turn, produces electrostatic forces (charges) in the medium around the electrodes (galvanically coupled). The free charges in the conducting medium are then free to mobilize and generate electrical conduction currents. To understand the electrostatic field distribution around the electrodes we solve the electrostatic problem for two electrodes placed in a nominal saltwater media (4 S/m). Figure 7 shows the resulting electrostatic field distribution.

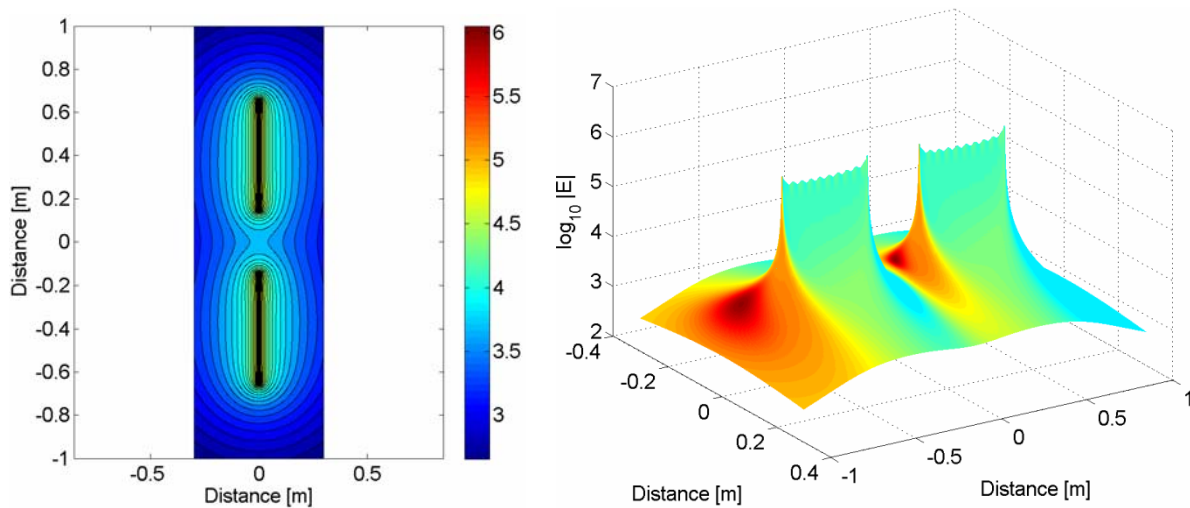


Figure 7. LEFT - Map view of the total electrostatic E field distribution between two 50 cm long by 1mm radius electrodes excited with a 1 V potential. RIGHT - 3D view of the field distribution showing that the total E field is much stronger on the electrodes than in the surrounding water.

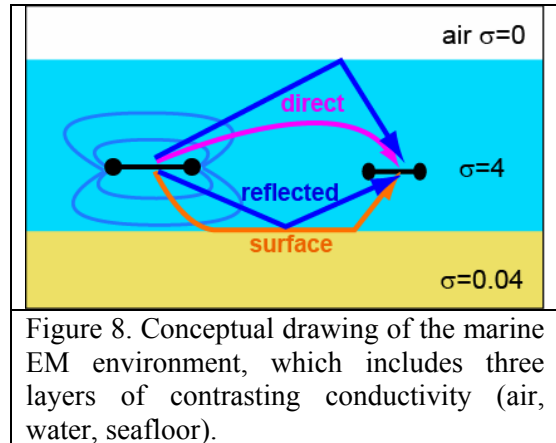
The E field from the electrodes falls off with the expected  $1/r^2$  behavior. Since the tangential component of the field vanishes on the electrodes and the normal component is proportional to the electric charge, we can conclude that most of the charge is located on the electrodes themselves. These charges produce potential differences between the electrodes and in the surrounding water that produce relatively strong currents. Therefore, we can also use the modified MAS code to calculate the current distribution around the electrodes. We compare current distributions in free space with those generated in water of varying conductivity. The interaction of electrodes in free space (air) is mainly through displacement currents (i.e., capacitively coupled), which are proportional to the time derivative of voltage and is thus small at low frequencies. When the same source is placed in water, the induced currents on the electrodes increase dramatically - over 6 orders of magnitude at 1 kHz. This increase is mainly due to the strong conduction currents

forming the return path between the electrodes and in the water medium.

These results indicate that strong conduction currents can be generated from an electric field source. These will generate strong E and B fields, which fall off as  $1/r^2$  from the electric field source as opposed to the  $1/r^3$  attenuation behavior from conventional induction loop sources.

### 2.1.2. Seafloor Interaction

Utilizing the general approach formed for understanding the E- and B-fields due to sources in an infinite conducting medium, we extend our analysis to better understand the interaction of source fields at and across the interface of varying conductivity layers. The transmitting dipole (electric or magnetic) emits VLF/LF electromagnetic signals that diffuse outwards both into the water column and downwards into the seafloor. Interaction with the sea surface and seafloor can both impact the total electric and magnetic fields in the water column where our receivers will be placed.



The full field solutions for a VLF/LF dipole source (electric or magnetic) contained within a conducting medium and surrounded by stratified layers of different conductivity are given by solving Maxwell's diffusion equations in terms of electromagnetic potentials. This theory is very-well established (e.g., Straton, 1941; Wait 1962; Chave and Cox, 1982; Ward and Hohmann, 1987; Born and Wolf, 1999). Consider the schematic model representation shown in Figure 8. This model accounts for three layers of varying electromagnetic properties: 1) the air layer – represented by a half-space of zero conductivity, 2) the water layer – a finite layer where conductivity is dominated by the fluid properties, and 3) the seabed – a resistive (less conductive than seawater) unconsolidated sediment layer where UWO reside. The illustrated signal paths between the source and receiver are (a) the response from the sea surface, (b) the direct field, (c) the surface (also termed “lateral” in some references) wave along the seabed, and (d) scattering from a UWO object embedded in the sediment layer.

The rate of decay in amplitude and the phase shift of the signal are controlled by both geometric and skin depth effects. Because the seafloor is generally more resistive than seawater, skin depths in the seafloor are longer; thus electromagnetic fields measured near the seafloor by a dipole receiver may be dominated by the components of the source field that have followed diffusion paths through the seafloor sediment. This effect is dependent of frequency and range.

For the transmission frequencies of interest for UWO applications, i.e. 100 Hz to 1 MHz, we must account for both diffusive and wave effects. As Loseth et al. [2006] point out, some care should be taken when considering the proper formulation for describing electromagnetic propagation in conductive media. Much of the theoretical and experimental work published for controlled source EM methods for hydrocarbon and seabed sediment exploration make simplifying assumptions due to the very low frequencies utilized. In some cases, a purely diffusive phenomenology is adequate to describe the electric and magnetic field distribution in the water column. It is also important to

consider the relative distance from the source (in comparison with the wavelengths and skin depths). In many cases, we can utilize the simplifying assumption that the near-field spherical-wave expression for the vector potential can be expanded into a spectrum of plane waves. This assumes that we are far enough from the source that plane waves and their interaction at planar boundaries are sufficient to describe field distributions. At the interfaces, a plane-wave constituent satisfies the boundary conditions which lead to the Fresnel reflection coefficients for the orthogonal polarization modes (TE and TM). For both modes, the “reflection” (diffusion) response from the layers is obtained by an iterative combination of the reflection (diffusion) and propagation in each layer. The total response within the source layer (the water layer) is determined by combining the responses from the layers above and below the source(s) and receiver(s). In sufficiently deep water and where the sediment layer is also deep relative to the skin depth, a double half-space model consisting of the water and sediment layers may be used as an approximate domain.

Although a thorough quantitative representation of source and scattered fields for UWO applications require 2D or 3D numerical modeling, the use of the 1D approximation provides considerable insight into the physics of marine E- and B-field propagation. In order to solve Maxwell’s equations for this case, we represent the magnetic flux-density vector  $\mathbf{B} = \nabla \times \mathbf{A}$  in terms of the vector potential  $\mathbf{A}$ . Analogously, the electric field intensity can be represented in terms of vector potential and its gradient. An infinitesimal dipole source can be represented by a length vector  $d\mathbf{l} \ll \lambda$  with current  $I(\omega)$ , leading to a source current density  $\mathbf{J}_0(\omega) = I(\omega)d\mathbf{l}$ . For such a source the vector potential is found by solving the Helmholtz equation  $\nabla^2 \mathbf{A} + k^2 \mathbf{A} = -\mu \mathbf{J}_0$ , where  $k = \sqrt{-i\omega\mu\sigma}$  is the wavenumber and  $\mu$  is magnetic permeability,  $\sigma$  is the conductivity, and  $\omega$  is the radial frequency:

$$\mathbf{A}(\mathbf{r}, \omega) = \frac{\mu I(\omega) d\mathbf{l}}{4\pi |\mathbf{r}|} e^{ik|\mathbf{r}|}. \quad (12)$$

The resulting field expressions can be derived in terms of complex integrals over a spectrum of plane waves.

Figure 9 shows an example of the superposition of the components of the electromagnetic field. In this case, we present the radial component of the electric field from a unit moment horizontal electrode source in seawater ( $\sigma_1=4$  S/m) over a resistive seafloor ( $\sigma_2=0.04$  S/m). The direct propagation imparts a component that dominates in the near field and attenuates exponentially due to the lossy nature of the medium and as  $1/r^2$  due to the geometric effect. When  $kr < 1$ , the direct field is significant and combines with the surface interaction component in an interference pattern, such that the resistive surface interactions (both for resistive seafloor and air interface) tend to absorb EM energy and reduce the total electric field.

The surface interaction component decreases as  $1/r^3$  for small ranges of  $r$  and  $1/r$  for larger ranges. The “dip” in the total field occurs at  $k_2 r = 1$  where the dominant component transfers from the

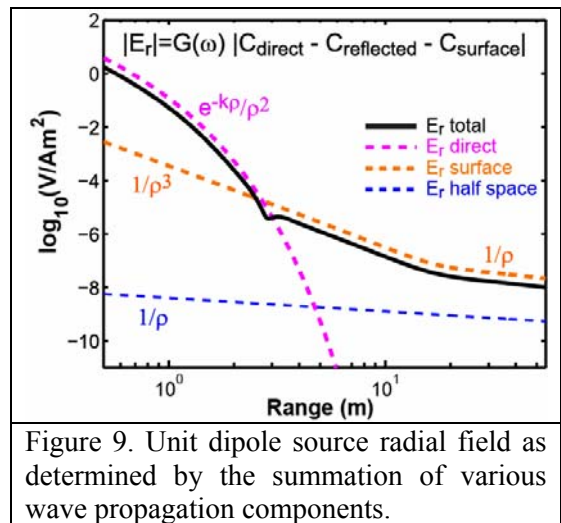


Figure 9. Unit dipole source radial field as determined by the summation of various wave propagation components.

direct field to the surface interaction fields. The “reflection” component from the existence of the halfspace generally falls off as  $1/r$  with range (when approximated using complex image theory). The exact closed form solutions derived by King et al. [1992] describe a near range half space response component decreasing as  $1/r^{0.5}$  at very short ranges and, then, as  $ik/r + (k_1^2/k_2^2 r^2)$  at larger ranges.

The full solutions are given by Chave and Cox [1982] and Loseth [2007] for electric field sources and by Cheesman et al., [1987], Dey and Ward [1970] and Coggon and Morrison [1970] and others for magnetic dipole sources. Chave [2009] has compiled a complete set (all combinations of dipole configurations) of closed-form solutions for both magnetic and electric sources in conductive media. We will utilize this formulation for understanding the propagation of magnetic and electric fields near the seafloor. These solutions present models for the various electric and magnetic sources in terms of complex Hankel transforms (integrals of kernel functions multiplied by Bessel functions of the appropriate Green’s function expressions). These integrals are solved by approximation or asymptotic solutions and can also be integrated numerically. The appendix summarizes the analytical expressions used and associated assumptions.

The effect of the seafloor below an electric field transmit-receive pair is shown in Figure 10. Model results were produced for both the in-line electric dipole-dipole and broadside electric dipole configurations using the model of Chave et al. [1986]. The magnitude and phase versus offset between transmitter and receiver exhibit significant differences when the system is in the presence of the seafloor relative to corresponding relationship in an infinite water column. The figures highlight the dominant paths of energy diffusion in the near-field region of the antenna. The solid and dotted curves represent the radial and azimuthal electric fields. Closest to the transmitter, the signal is dominated by the direct propagation and falls off exponentially. At ranges below about one skin depth ( $z = \sqrt{2/(\omega\mu\sigma)}$ , in this case  $\sim 1.25$  m), the source looks like a quasi-static dipole and the attenuation of the horizontal electric field is controlled by the conductivity of the water column. At ranges greater than a skin depth, the effect of the less conductive seafloor half-space becomes noticeable. At much larger ranges or in very shallow water, the presence of the sea-air interface will also become a significant factor. Under these conditions the electric field response is dominated by a  $1/r^3$  falloff in

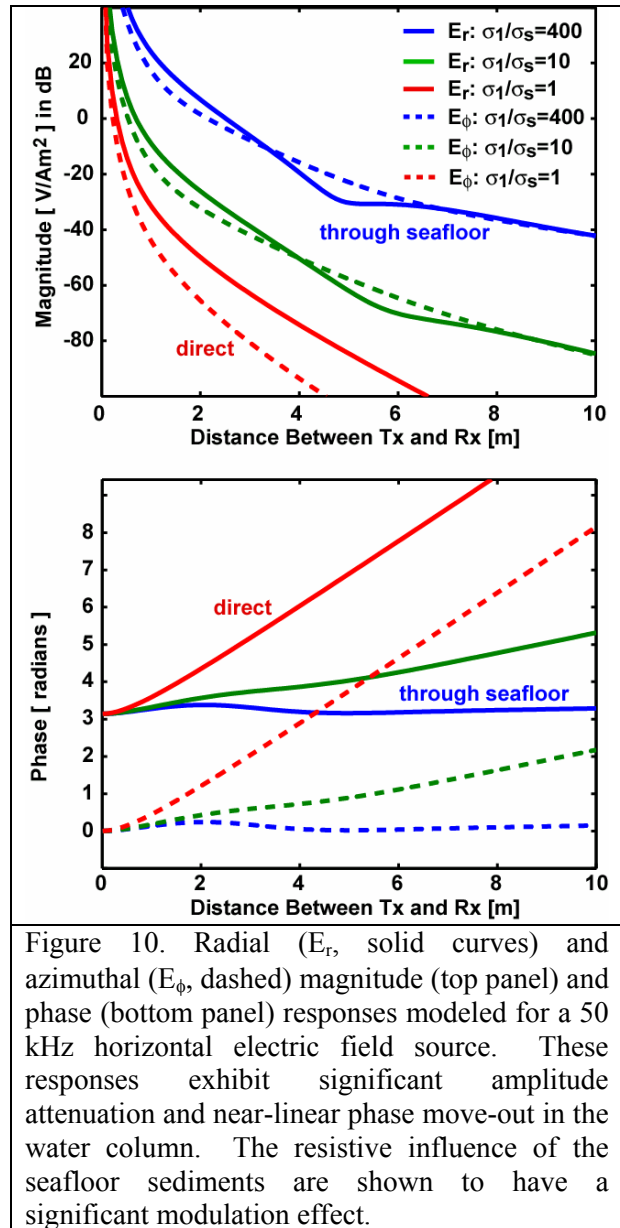


Figure 10. Radial ( $E_r$ , solid curves) and azimuthal ( $E_\phi$ , dashed) magnitude (top panel) and phase (bottom panel) responses modeled for a 50 kHz horizontal electric field source. These responses exhibit significant amplitude attenuation and near-linear phase move-out in the water column. The resistive influence of the seafloor sediments are shown to have a significant modulation effect.

amplitude and is associated with nearly constant phase.

Similar “move out” plots for both vertical magnetic (VMD) and horizontal electric dipole (HED) sources are shown in Figure 11. Comparisons can be drawn between low (1 kHz) and high (100 kHz) end-member transmission frequencies as well as for varying conductivity contrast between seawater and the underlying seafloor. Despite the effect of the surface interaction with the seafloor at ranges greater than 4-10 meters, we observe significant attenuation. In fact, we would not expect any current sensor (E or B) to resolve signals at <-150 dB. We also note that the different components of E and B fields tend to be affected differently by the existence of a resistive halfspace. For instance, the radial magnetic field component from the VMD source reveals noticeable differences in the response from low and high conductivity contrast at shorter ranges when compared to other components.

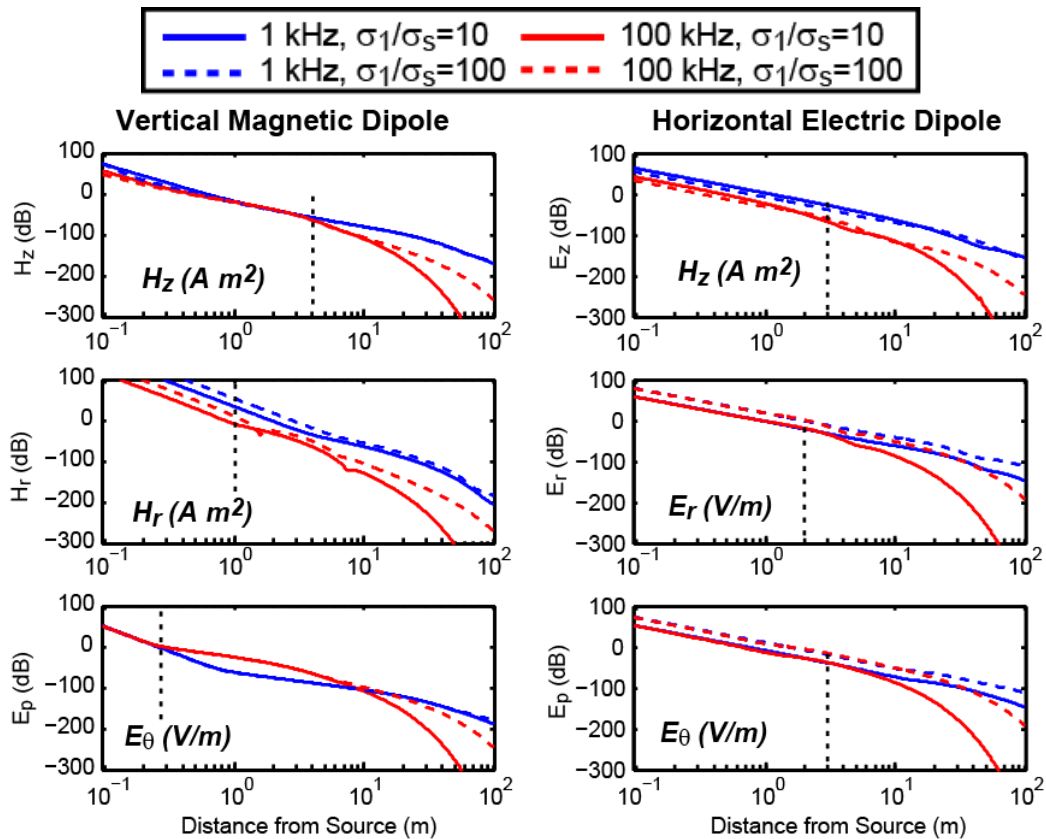


Figure 11. Field intensity versus range from source. Solid lines correspond to a relatively low conductivity contrast between the seawater and the seafloor; dashed lines correspond to a higher contrast.

To fully capture the sensitivity of our model to changes in seafloor conductivity (or conductivity contrasts) over the range of relevant EM frequencies, we compute the effect of a +/- 0.1 S/m perturbation in seafloor conductivity from the mean value of 0.4 S/m. The conductivity of the water column is 4 S/m and air is 0 S/m (Figure 12). The sensitivity is represented by the change in field value with change in seafloor conductivity. Figure 13 shows the range-frequency space sensitivity for the horizontal electric dipole source elevated 2 meters above the seafloor. From this analysis we see that the radial magnetic and tangential electric fields attain a maximum value at frequencies of ~2 kHz and ~10 kHz, respectively. The vertical component of the magnetic field falls off with frequency.

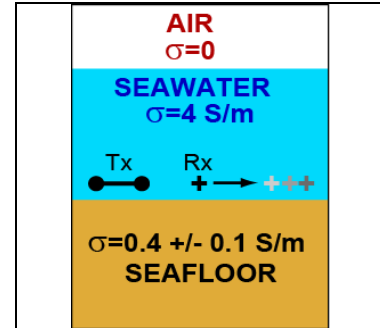


Figure 12. Model structure for electric dipole over a resistive seafloor.

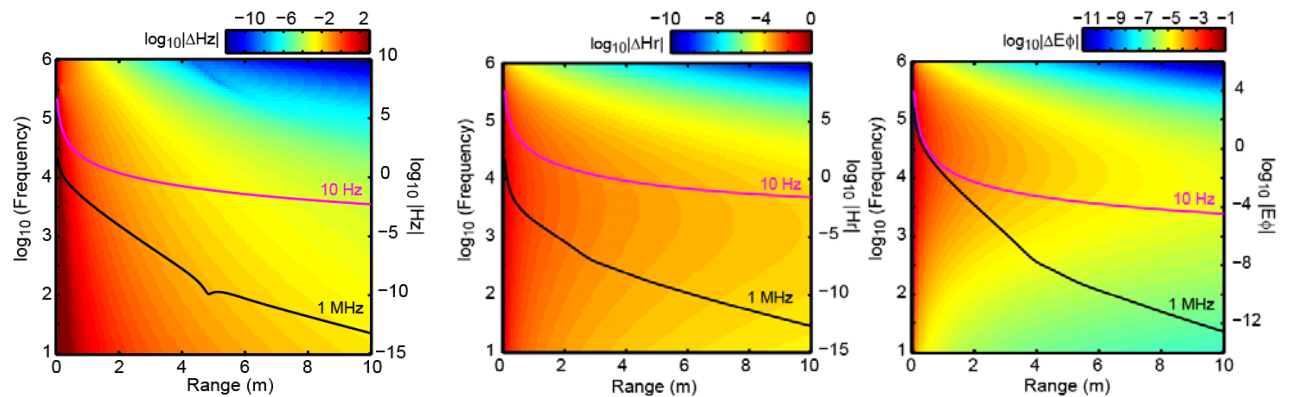


Figure 13. Sensitivity analysis for E and B field components to +/- 0.1 S/m perturbation to a resistive seafloor at varying frequencies and range offsets.

Now if we add a highly conducting layer, or the equivalent of a one-dimensional target, we can assess the influence of a simulated metallic target using this model. We use the recursion relationship from Key (2009) for computing the transform kernel (Hankel transform) of the vector potential for a HED transmitter. This extends the 1D model to account for interaction across  $N$  layers. All components of E and B are calculated.

In our case started with the conductive sandwich configuration and added a thin very conductive layer (4-layer model) in the resistive seafloor halfspace. The model structure is shown in Figure 14. Although the layer interaction is highly dependent on signal frequency, Figure 15 shows the effect of the anomalous conductive layer (the target) on the background layered (air-sea-seafloor) response for 50 kHz broadside and in-line HED configurations. Figure 15 also shows how the anomalous field varies with range from the transmitter. The anomalous field is simply calculated from the ratio of the total field to that of only the background natural media. This illustrates the variability in sensitivity of the E and B field components for both configurations to the inclusion of a buried conductor.

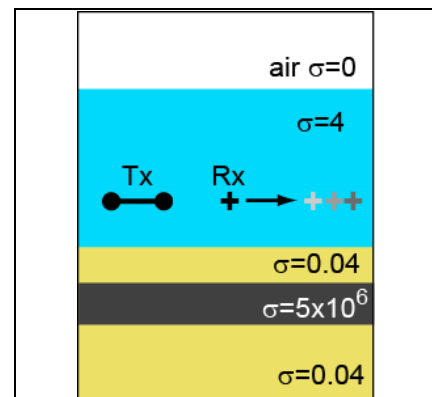


Figure 14. Model structure for 1D buried target modeling.

The broadside and in-line configurations generate different anomalous field "move-out" forms. For the broadside configuration the perpendicular (denoted  $E_y$  here) electric field component yields the strongest response, but the vertical magnetic field is most sensitive to the conductive anomaly in the near range (<6 m). For the in-line configuration, the electric field components generate the strongest response with weaker overall responses from the orthogonal magnetic component. Strong near range anomalous signals are observed for both the magnetic and electric field components.

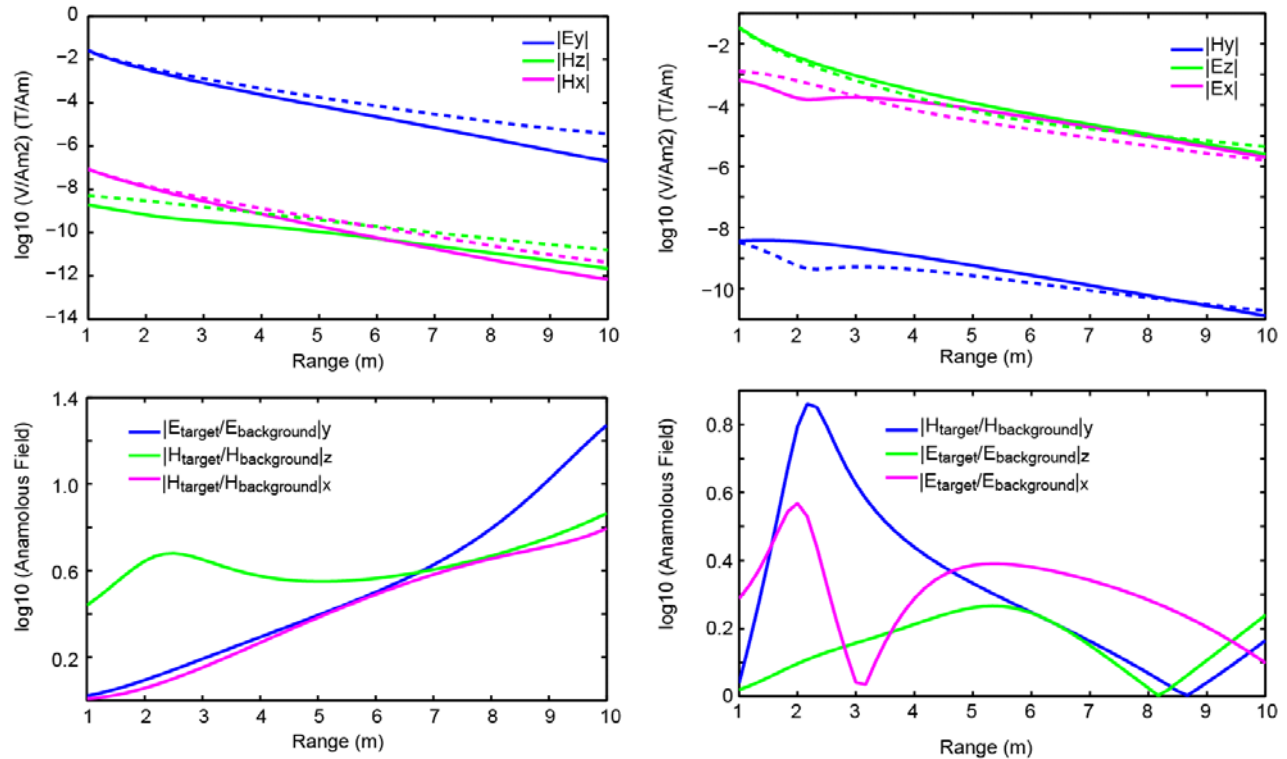
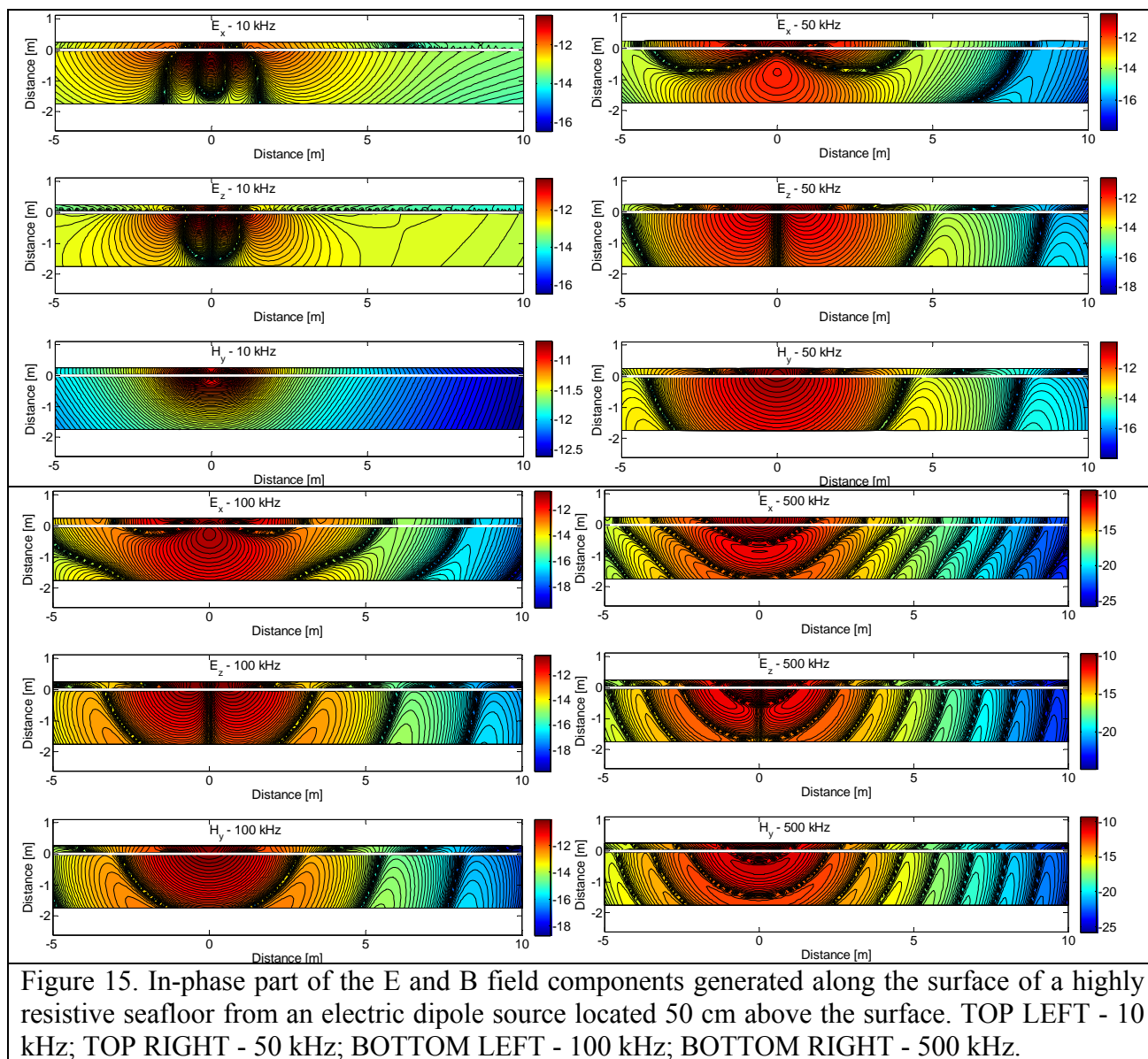


Figure 14. E and B field components and their attenuation with range in the water column over a resistive seafloor with embedded conductivity anomaly. See Figure XX for the geometry of broadside and inline configurations. The top plots show the background field components modeled for the 3 layer case absent of the highly conductive layer and the dotted curves show the total response with the conductive layer. Bottom plots show the anomalous fields from the inclusion of the conductive layer. LEFT – Broadside configuration E and B field components due to a 50 kHz electric field unit dipole transmitter. RIGHT – The field components for the in-line configuration.

Full two and three-dimensional modeling of surface interaction was also simulated using numerical boundary integral methods, i.e., the MAS. Figures 15 show the in-phase part fo the total magnetic and electric field components from a HED source located 50 cm above the seafloor. The conductivity of the seafloor was to that of air to reflect the endmember resistive case and to accentuate the surface interaction effects. The results show that at low frequencies there is little evidence of surface reflections or significant surface interaction. At 100 and 500 kHz the model

yields strong inducted surface waves along the boundary.



### 2.1.3. Target Scattering

The detection and localization of submerged objects in conductive water relies on our ability to sense scattered fields induced by either magnetic or electric primary fields. Here we consider the response from compact metallic objects using both analytical and numerical (MAS) modeling techniques.

This classic EM induction problem has been presented and discussed for terrestrial UXO applications for many years. For the case of submerged objects, a number of additional considerations must be accounted for. The finite conductivity and dissipative nature of the source medium causes significant attenuation of the field with distance from the source. In addition, the scattering from objects in a conductive medium should fully account for the interaction of the magnetic and electric fields, as the electric field component is significant, unlike the terrestrial case.

Analytical models assume uniform fields over the spatial extent of the compact objects of interest. We utilize axisymmetric canonical representations to simplify the frequency response function. A dipole approximation is used to estimate the backscattered electric and magnetic fields such that the electric and magnetic dipole moments of the object are obtained from the polarizabilities. The resulting scattered electromagnetic field may be approximated by that from the superposed equivalent transverse electric and magnetic dipoles if the dimension of the object is much smaller than a wavelength in the seawater medium and the distance to the computed field point.

Based on the strength of the incident field, an conducting object will acquire a induced electric dipole moment:  $P(r, \omega) = (\epsilon + \sigma / i\omega) \alpha_E (\mathbf{E}(r, \omega) \times \mathbf{n})$ , where  $\alpha_E$  is the electric polarizability of the conducting object and  $\mathbf{n}$  is the unit normal vector of uniform flux across the object parallel to angle of incidence. The current moment can be derived by multiplying by  $i\omega$ , so that the induced electric current moment is in phase with the incident electric field.

The incident magnetic field is also assumed uniform in this case, so that the conducting object will have an induced magnetic dipole moment in opposite direction to the inducing magnetic field:  $M(r, \omega) = -\alpha_M (\mathbf{H}(r, \omega) \times \mathbf{n})$ , where  $\alpha_M$  is the magnetic polarizability. The electric and magnetic polarizabilities are functions of the volume and shape of the conductive object as well as its relative orientation with respect to the inducing field.

The scattered field is determined first by simulating the incident field at the location of the scattering object, and then generating the surface currents and representing them as magnetic and/or electric dipole moments. Reflections between the scattering object and the surface of the conducting medium must be accounted for. We consider cases when the object is in an infinite conducting medium and when it is buried beneath or lying on a resistive seafloor.

For the case of a sphere excited by a VMD source in an infinite medium we start from the classical analytical formulation of Wait [1951]. This solution is extended to account for the finite conductivity of the medium and interaction of E and B field components. We utilize the solution in terms of the scattered vector potential:

$$\mathbf{A}^s = \frac{\mu}{4\pi r^3} \left( \frac{1+k_2 r}{1+k_2 a} \right) e^{-k_2(r-a)} (\beta \mathbf{H} \times \mathbf{r}), \quad (13)$$

where the frequency response of a sphere can be represented by

$$\beta(\omega, a) = 2\pi a^3 \frac{3\mu(k_1 a \coth(k_1 a) - \mu(k_1 a)^2)}{\frac{(k_2 a)^2}{1+k_2 a} [k_1 a \coth(k_1 a) - 1] + \mu(k_1 a)^2}, \quad (14)$$

where  $a$  is the radius of the sphere. Similar response functions can be formulated for flat plates and solid cylinders. The magnetic and electric fields can then be obtained from the vector differential equations:

$$\mathbf{H} = \frac{1}{\mu} \nabla \times \mathbf{A} \quad (15)$$

$$\mathbf{E} = \frac{i\omega}{k^2} \nabla \nabla \cdot \mathbf{A} - i\omega \mathbf{A}. \quad (16)$$

For the case of a cylinder on the surface of a resistive half space excited by a HED source, we follow a similar formulation. We consider a cylinder of length  $2h$  and radius  $a$ . The incident electric field at the object can be determined by evaluation of the source field propagation, as described previously. From this the axial induced current can be determined:

$$I(r) = \frac{-i4\pi}{\omega\mu} \mathbf{E} \left( \frac{\cos(k_1 r) - \cos(k_1 h)}{\chi \cos(k_1 h) - k_1^2 h^2 - i \frac{2}{3} k_1^3 h^3} \right), \quad (17)$$

where the response function

$$\chi(\omega, a) = 2 \ln(2h/a) - 3 + \frac{5}{12} k_1^2 h^2 + i \frac{2}{9} k_1^3 h^3. \quad (18)$$

Therefore, for an x-directed electric field dipole with moment  $P(x) = 2hI(x)$  generates a scattered field:

$$E_x(\omega, r) = \frac{i\omega\mu P(x)}{4\pi k_1^2} \left[ \left( \frac{k_1^2}{r} + \frac{ik_1}{r^2} - \frac{1}{r^3} \right) - \frac{3x^2}{r^2} \left( \frac{k_1^2}{3r} + \frac{ik_1}{r^2} - \frac{1}{r^3} \right) \right] e^{ik_1 r}, \quad (19)$$

where  $r$  is the distance from the center of the dipole.

Figure 17 shows an application of these analytical scattering models for a VMD source and 10 cm diameter sphere in a conducting medium. The transmitter and receiver are separated (slingram type) by 1 m and offset 1 m from the conducting sphere.

Profiles over the sphere show the real part of the scattered vertical component of the magnetic field as the transmitter-receiver pair traverse over the sphere as well as the imaginary part of the transverse component of the electric field. At the lower frequency (5 kHz) the scattered magnetic field dominates the response with a maximum of  $\sim 6 \mu\text{A}/\text{m}^2$ , but the electric field is noticeable and not insignificant. At the higher frequency of 50 kHz the magnetic field is reduced due to the increased wavelength attenuation, but the electric field is relatively much stronger (note the plots are consistently 10:1 in H:E strength).

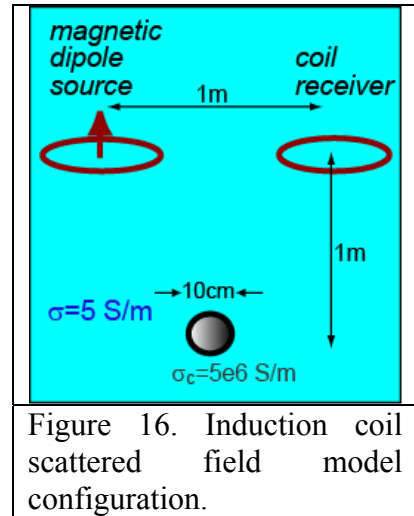


Figure 16. Induction coil scattered field model configuration.

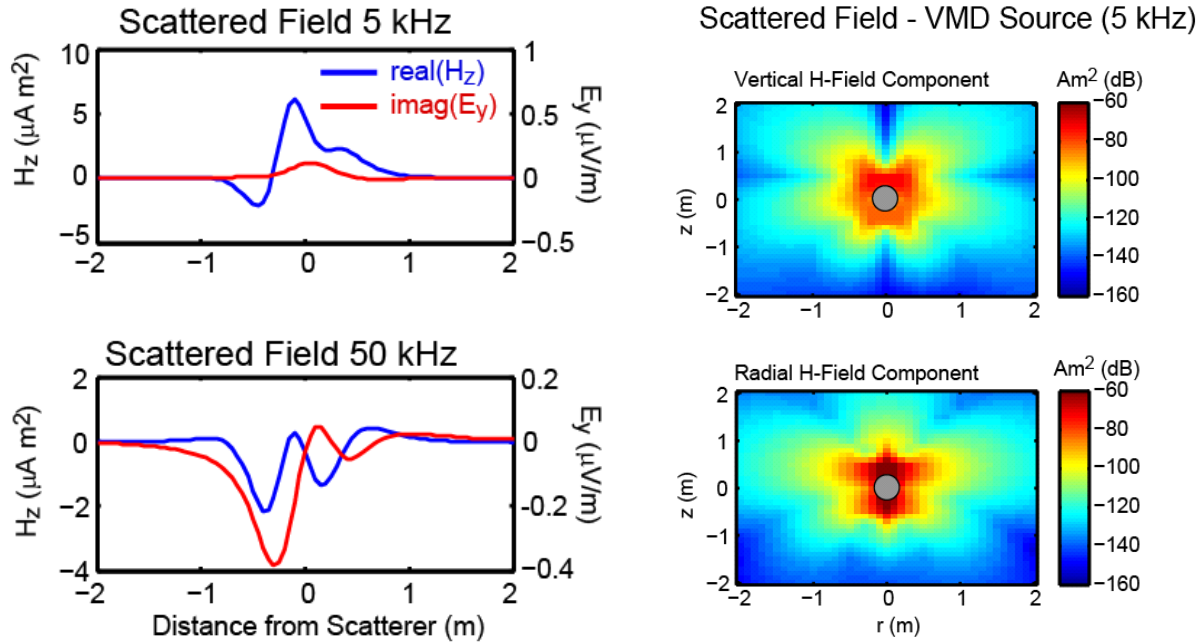


Figure 17. LEFT – Profiles over the scattered magnetic (blue) and electric (red) fields from a solid steel sphere ( $\sigma=10^6$  S/m,  $\mu=150$ ). RIGHT – Scattered field distributions around the sphere; magnetic field components only.

The scattered electric field distribution over a steel cylinder resting on the surface of a resistive halfspace also yield fairly complex spatial patterns. In Figure 18 we show the electric field components for a cylinder with its primary axis oriented at 30 degrees from that of the modeled electrode transmitter. This generates nearly equivalent radial and tangential scattered fields using the coordinate reference frame of source electrode. Relatively strong and likely measureable secondary E fields are observed at distances up to 2 m on either side of the target scatterer.

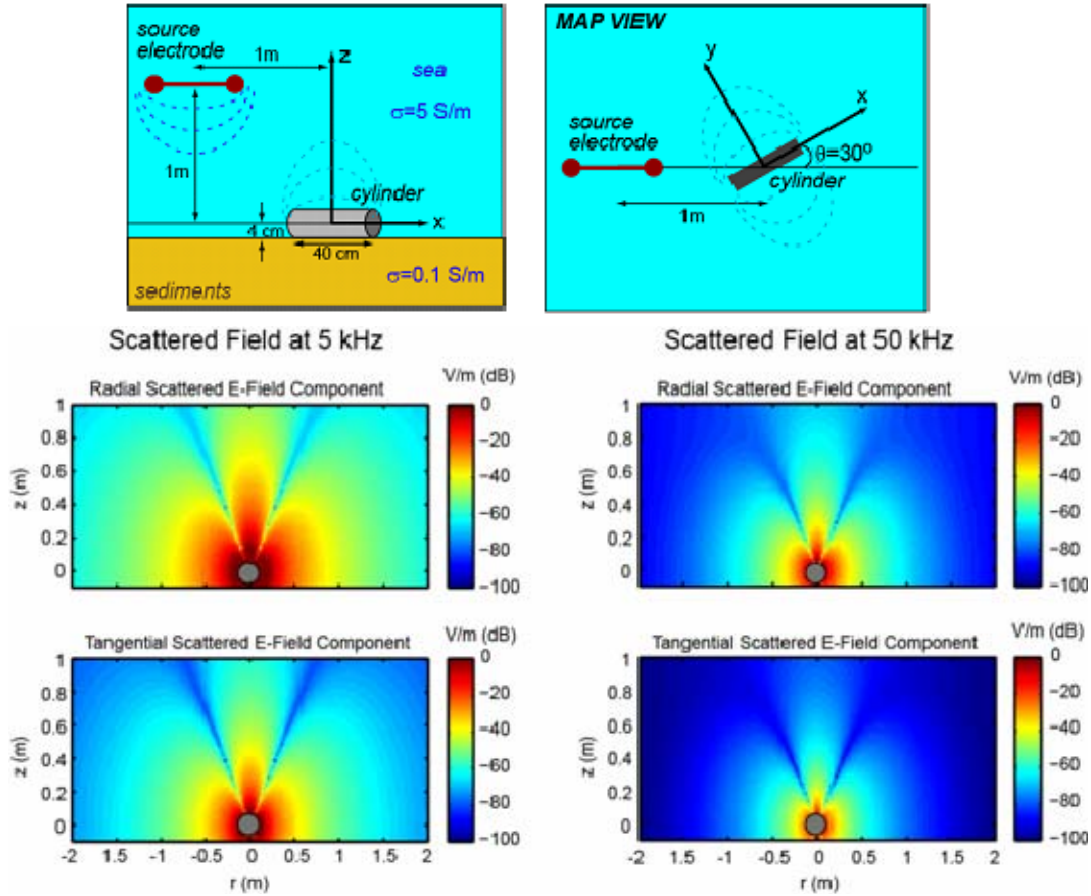


Figure 18. Electric field scattering for a finite length (40 cm long X 8 cm diameter) steel ( $\sigma=10^6$  S/m,  $\mu=150$ ) cylinder as excited by a unit electric dipole source 1 m above and 1 m offset. The field components are nearly equivalent because of the orientation of the primary electric dipole moment of the cylindrical scatterer, which is oriented along its long axis.

To further characterize and compare the scattering from targets excited by electric and magnetic field transmitters, we combined the extended MAS models developed by Shubitidze (UX-1632) with the new E and B field source models described previously. Here we investigate the secondary magnetic fields from a conducting and permeable sphere in a conducting saltwater host medium. Figures 19 and 20 shows profiles across the plane of the transmitter for the vertical and lateral magnetic field components scattered from a 10 cm diameter sphere with conductivity of  $4 \times 10^6$  S/m and magnetic permeability of 100. The B field source is comprised of a 1m X 1m induction loop transmitter and the electric field dipole is represented by two 1 m segments of bare wire.

Comparisons of the scattered magnetic fields generated from an E field source relative to a B field source are shown. Equivalent power from a 1 A input current is used to simulate the incident source field, which in turn, generates the scattered fields. At a source-target offset of 1 m, the two sources lead to scattered magnetic fields of roughly the same strength. However, as the transmitter moves further away from the target (i.e., increasing range), the E field source tends to generate stronger scattered magnetic fields. We mainly attribute this to the increase in the source field strength incident on the target from the E field source relative to the B field source. This

provides evidence of the potential for an e field source to improve target range for UWO. In the next section we validate these model results through controlled data collection.

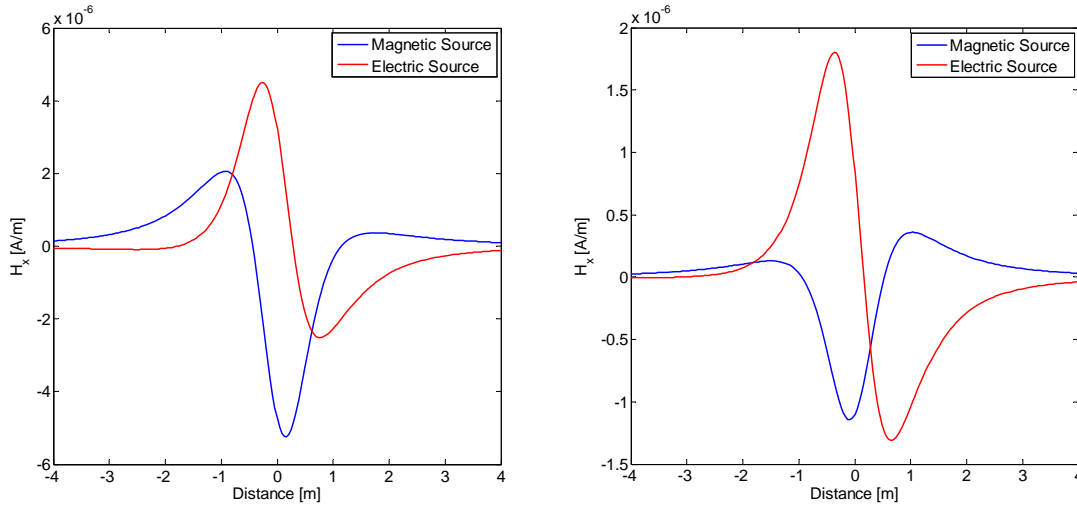


Figure 19. The lateral component,  $H_x$ , of the magnetic field scattered from a 5 cm radius steel sphere. LEFT - The center of the source electrode (red) and induction coil (blue) are both centered at -1 m from the target. RIGHT - The center of the E and B field transmitters are offset -2 m from the target.

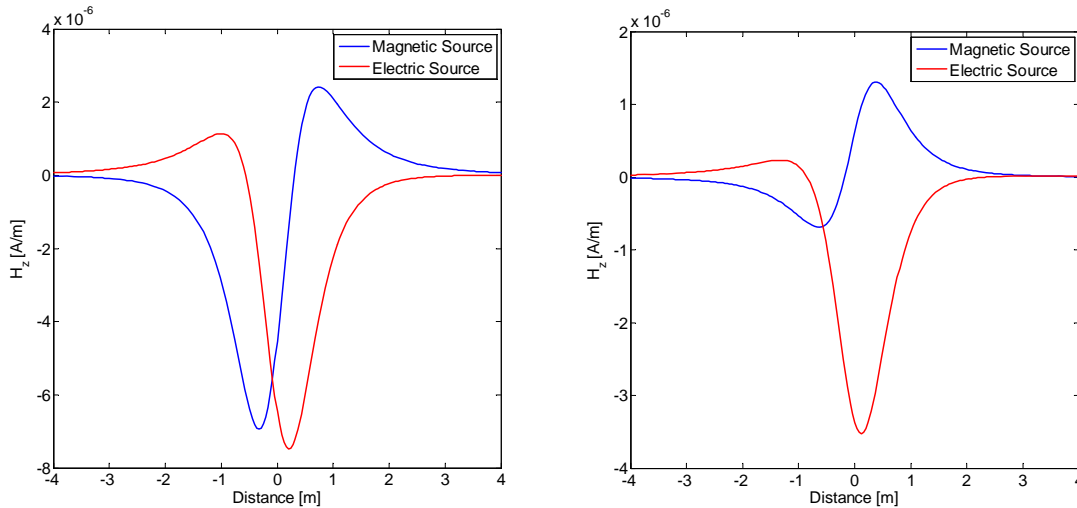


Figure 20. The vertical component of the magnetic field scattered from a 5 cm radius steel sphere. LEFT - The center of the source electrode (red) and induction coil (blue) are both centered at -1 m from the target. RIGHT - The center of the E and B field transmitters are offset -2 m from the target.

## 2.2. Task 2 - Controlled Data Collection and Experimentation

The primary purpose of this Task was to provide an experimental basis for comparison and validation of modeling and simulation performed in Task 1. Of equal importance was the evaluation of the practical capabilities and limitations of commercially available transmitter and receiver systems. After initial research and sensor assessments, we downselected and conducted preliminary data collections and investigations with marinized electric field sensors under controlled laboratory conditions. Subsequently, we collected data in an open water environment with both electric and magnetic field transmitters and receivers.

### 2.2.1. Electric Field Laboratory Data Collection

In Fall 2010 we conducted preliminary laboratory investigations using an existing potted electrode receiver developed by Information Systems Laboratory (ISL). These receivers are very high sensitivity (nV-level) and have been and are currently being deployed for Naval surveillance operations. ISL has deployed the fundamental OEM (original equipment manufacturer) sensing elements and data acquisition systems in seafloor monitoring modules, sonobuoys, and port and harbor security sensor networks. Descriptions of the electrodes and summary assessments of their performance are given in the following section.

Experiments were conducted in a controlled environment in a small, 3.1m x 1.2m x 1.2m (LxWxH) non-conducting saltwater test tank. The basic layout and photos of the tank are shown in Figure 21. Periodic measurements of conductivity, salinity, and temperature ensured that a stable environment was achieved. Measurements of conductivity of the saltwater in the tank varied from 5.20 to 5.24 S/m throughout the data collection.

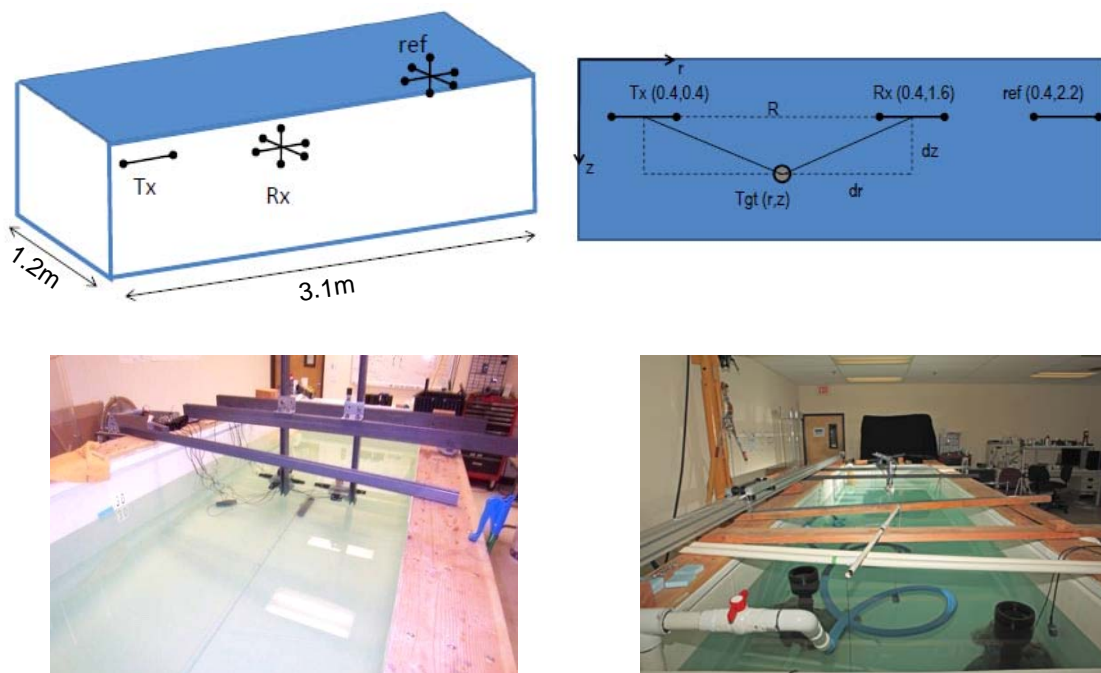


Figure 21. Saltwater tank set up used for initial electric field sensor characterization and data collection. The non-metallic, non-conducting tank was constructed specifically for controlled testing of E field sensors. Water conductivity was measured throughout testing and remained at ~5.2 S/m.

Data were collected with a set of 3-axis Ag/AgCl electrodes submerged in the small saltwater tank (Figure 22). A short silver electrode was used as a source and delivered milliVolt level inputs to the tank. Although the source was limited to these very low power levels, direct transmission of the electric field was observable at all distances (up to 3m from the source; limited by the size of the tank). Experiments were also conducted to record the scattered electric field from various metallic targets using 1kHz square wave input as well as a swept-frequency sinusoidal input. Due

to the limitations of the source, we found it generally difficult to observe scattered signals, but secondary fields as high as 7dB above the background noise (5-15 nV) we recorded.

Experiments were conducted with the source excited by a narrow-band (single frequency sinusoid) continuous wave input as well as a 20 ms square wave. Direct transmission from the source electrode to the receivers reveal detectable signals that range from 200 nV to over 90 mV. Noise levels in the laboratory ranged from 5-15 nV.

Experiments were also conducted to record the scattered field from various metallic objects (solid steel spheres and rods). Using a 1 kHz sine wave input to a source electrode located 30-50 cm from the target. We recorded the received signal in 2 sets of 3-axis electric field sensors. Power spectra of the raw receiver voltages showed a small, but discernable target signal above the background noise. These signals ranged from +0.7 dBV in the x-axis receiver to +7 dBV in the z-axis receiver.

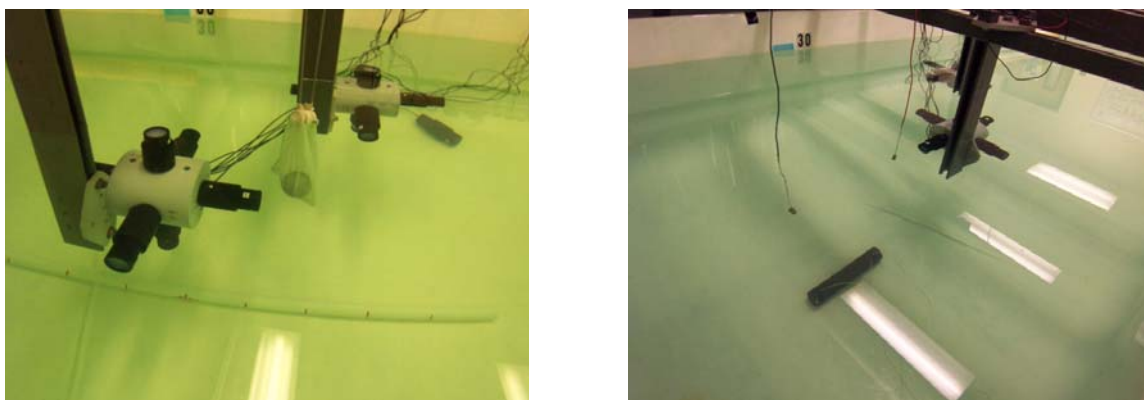


Figure 22. Photographs of the ISL 3-axis E field sensors during target scattering experiments. Steel spheres and solid cylinders were used as test target stimulants.

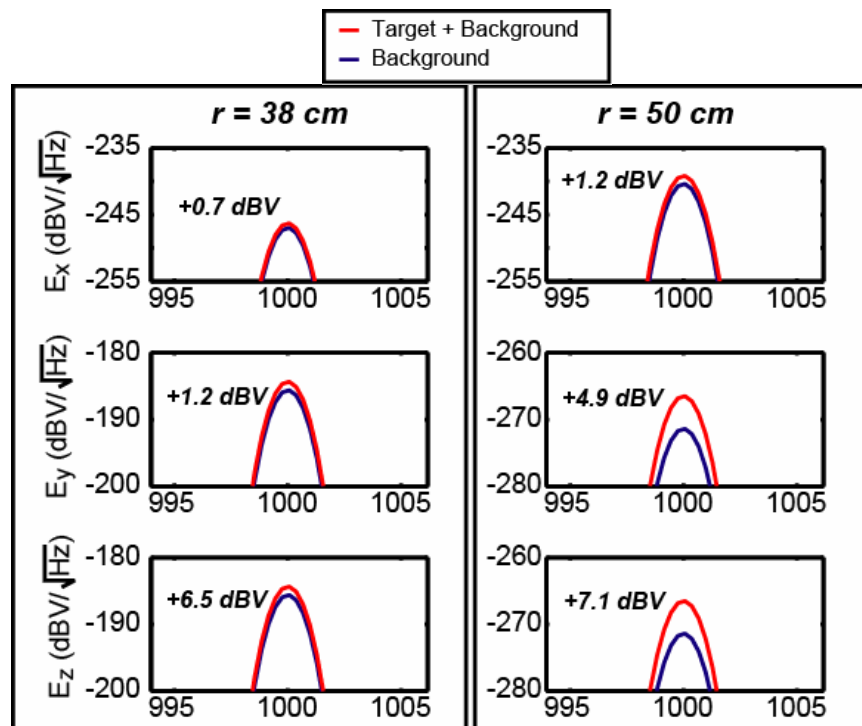


Figure 23. Spectral estimates of demodulated electric field signals. Background and target signals are shown for frequency domain measurements at 1 kHz excitation. Very small, but measurable target excitation was observed. Signals were severely limited by small input voltages applied to a small transmitter electrode in the tank.

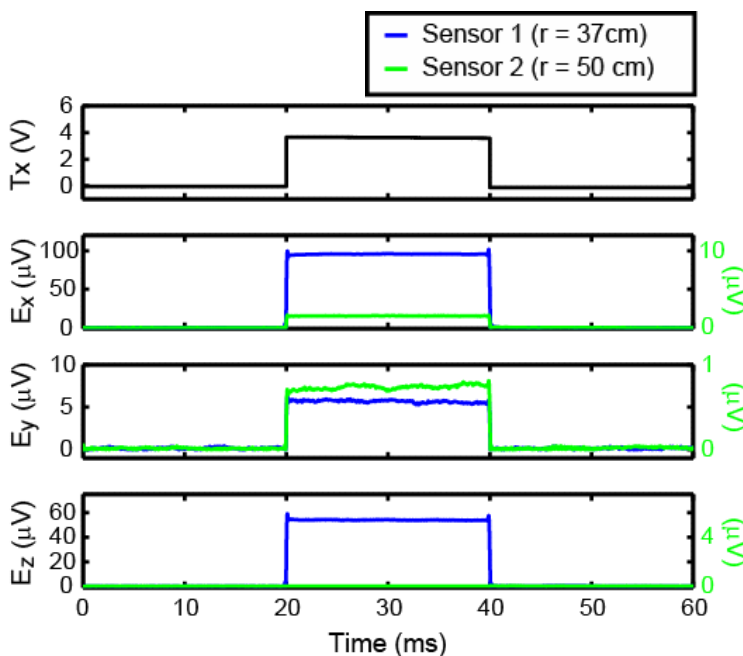


Figure 24. Examples of time domain electric field data collection using a 20 ms square wave input. Small electric field signals were observed on the order of a few parts-per-million (or microVolts). Noise levels during these measurements were 5-15 nV or on the order of 1 part-per-billion.

### 2.2.2. Open Water Experiments

In order to gain some freedom from the constraints of testing in a water tank and to eliminate the effects of noise associated with the laboratory environment we performed a series of experiments in an open water environment. The overall purpose of testing electric and magnetic field sensors in this open water area was to develop fundamental understanding of sensor responses to this environment, to metal targets of interest, and to proximity to the seafloor or air-sea interface. Specific goals included:

- provide data to help validate/verify analytical and numerical modeling of E- and B-field sensors responses
- observe small scale (1-10 meters) range attenuation for both electrode and induction coil sources
- provide data for evaluating the information content from scattered E and B- field signals (with respect to characterization of UXO)
- provide baseline for future measurements toward focused sensing design (in Year 2)

Data were collected in shallow water (1-3 meters) near a dock facility off Okaloosa Island, Florida in the Choctawhatchee Bay (see Figures 25 and 26). Data acquisition and power were supplied topside and utilized the dry environment of the dock. Water temperatures ranged from 8.9 to 9.7 C. Pressure, temperature, and conductivity were measured with a handheld CTD sonde (YSI Castaway). Raw data were acquired every 200 ms during depth casts from the dock equating to a approximate depth resolution of 0.015 decibars. These data were processed and averaged to yield pressure depth, conductivity and specific conductance, salinity, sound velocity, and fluid density. Figure 27 shows data from two casts off the dock before and during our experiments. The conductivity in this area, ~2.6 S/m, is lower than that of ocean water due to freshwater inputs upstream in the bay. Water temperatures generated a need for wetsuits for personnel working in the water during experiments.



Figure 25. Location map showing area in Choctawhatchee Bay where controlled data collection was conducted.



Figure 26. Photographs of the dock site from which data collection was facilitated. The seafloor consisted of fine sands and silt and had very little variation in relief. Water depths ranged from 1 to 3 meters over the site. Semi-diurnal tides of 14-27 cm did not influence water depths significantly.

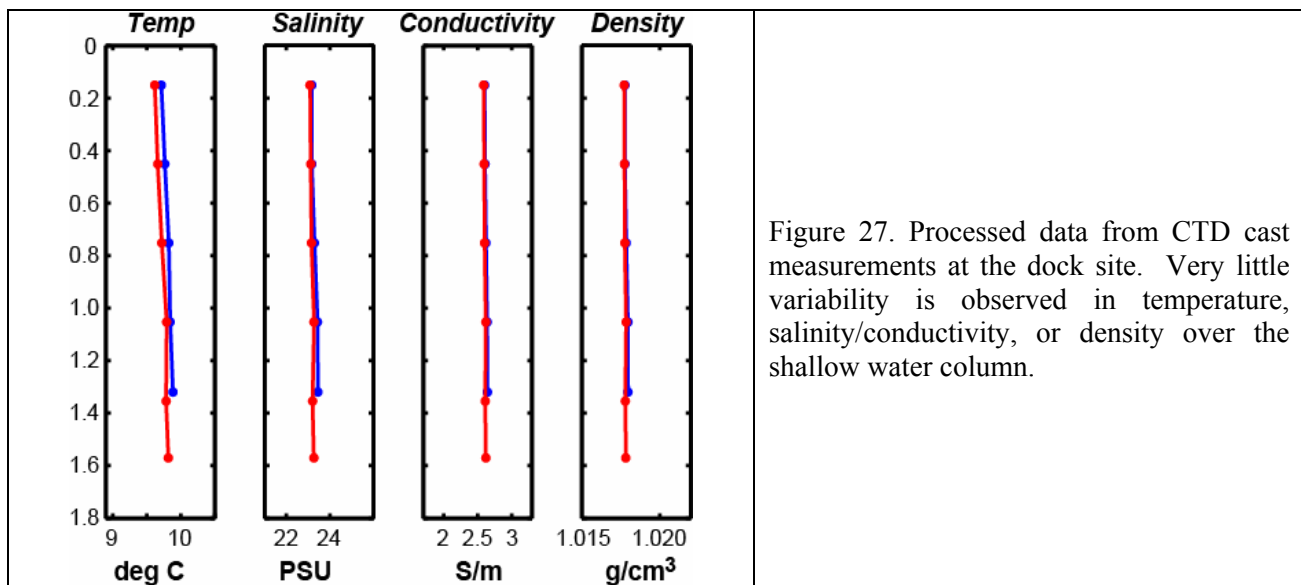


Figure 27. Processed data from CTD cast measurements at the dock site. Very little variability is observed in temperature, salinity/conductivity, or density over the shallow water column.

For this data collection we applied both electric and magnetic field sources. The magnetic field source consisted of a 1m x 0.5m custom wound induction coil comprised of a 10 turns of 16 gauge single strand, insulated, copper wire. The electric field source consisted of a pair of 8cm diameter by 40 cm long graphite electrodes. For an electric field receiver we used the Ultra Electronics PMES Ag/AgCl electrodes and integrated ultra low-noise pre-amplifiers. The magnetic field receiver used was the KMS Laboratory for Electromagnetic Innovation (LEMI) LEMI-134 wideband B-field sensor. This sensor is capable of resolving magnetic fields of a few hundred picoTesla over the frequency range of 17Hz to 280 kHz. Details of the Ultra E-field and LEMI B-field sensors are given in the Appendix.

We also acquired baseline data with two commercial terrestrial EM systems by encasing them in a sealed pressure vessel. We acquired data with the Geophex GEM-3 frequency-domain EM system and the Geonics EM-61 MkII pulsed induction (time domain) system. Photographs of the systems

used are shown Figure 28.

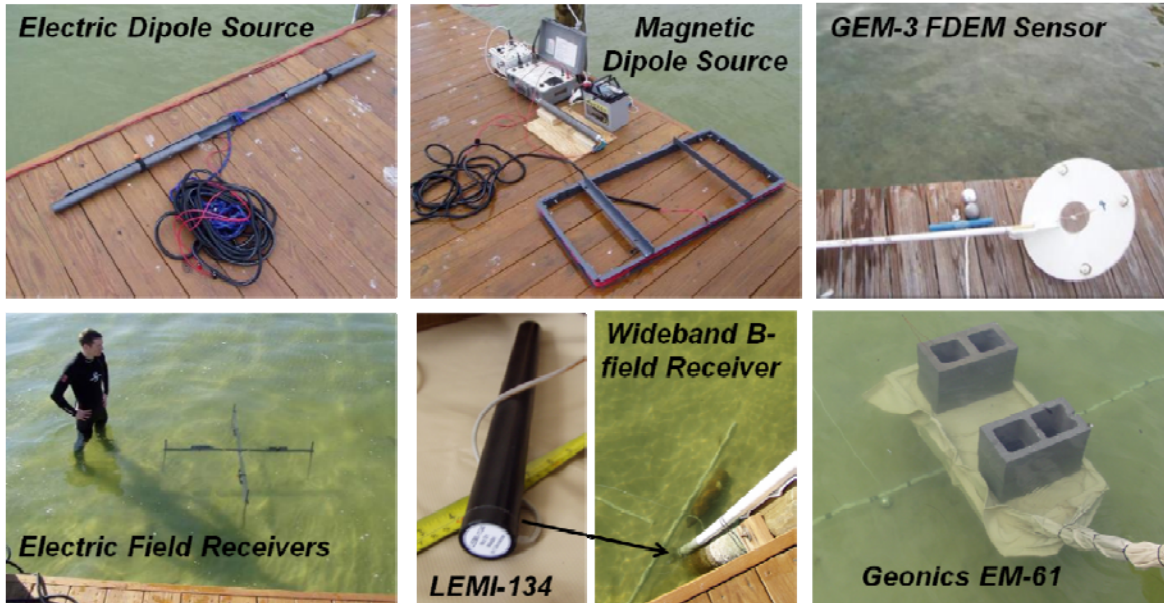


Figure 28. Photographs of the marinated sources and receivers used for data collections.

E- and B-field transmitters were driven with the Zonge ZT-30 transmitter from a set of 12 VDC batteries. The basic set up of these experimental systems are shown in Figure 29. A square wave current excitation was used for both transmitters generating the E- and B-field signals showing in Figure 30. The electric dipole source reflects E-field signals that are proportional to the gradient of the voltage potential across the electrodes. The magnetic dipole source generates E-field signals that are proportional to the time rate of change of the vector potential rotational magnetic field. The primary E-field signal source for the horizontal electric dipole are galvanically driven currents, whereas the primary E-field signal from the vertical magnetic dipole is driven by inductively coupled currents.

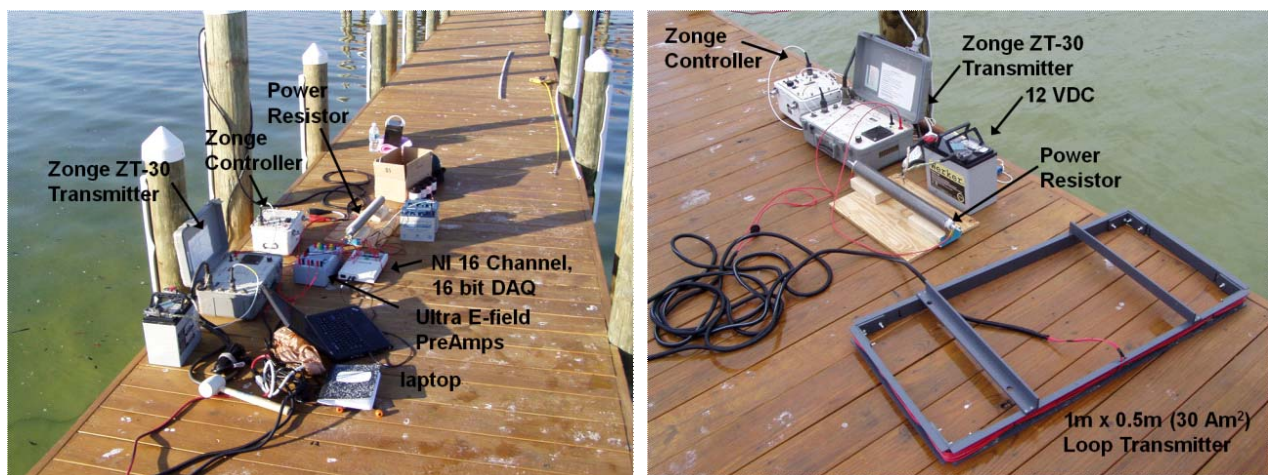


Figure 29. Basic dock-side set up and equipment used for preliminary E- and B-field data collection. A 16 channel, 16 bit National Instruments data acquisition system was used for high resolution analog-to-digital conversion at data rates up to 1 MHz from E- and B-field sensors.

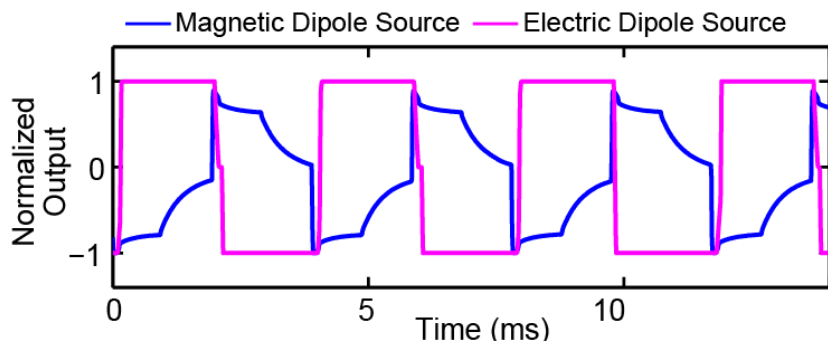


Figure 30. Normalized output from the E-field electrode sensors driven by either a vertical magnetic dipole (blue) or horizontal electric dipole (magenta) source transmitter.

Among our most notable results from these experiments was the relatively strong magnetic fields detected in the wideband induction coil B-field sensor at distances >2m from the transmitter. We acquired data using the B-field sensor as a function of distance from the transmitter. The HED source drew an average current of 6 A at 12 VDC while the VMD drew about 8 A at 12 VDC. This equates to total resistance of 2 Ohms for the HED source and 1.5 Ohms for the VMD source. This matches our estimates of 2.2 Ohms for the electrode source given the length (40 cm), cross-sectional area (0.067 m<sup>2</sup>), and water resistivity (0.38 Ohm-m).

The HED and VMD transmitters were submerged in the water column at various depths from the water surface to the seafloor. The transmitters were held stationary in place while the B-field receiver measuring the total vertical magnetic field was systematically moved from 2 m out to 7.5 m away from the center of each transmitter type. Within 2 m the receiver sensor data recorded maximum voltage values and was clipped. Signal attenuation was sufficient to record raw voltage output of over 1 V out to 5 m for both source types. These surprisingly strong magnetic fields exceeded our expectations. Raw normalized voltage output values are shown in Figure 31.

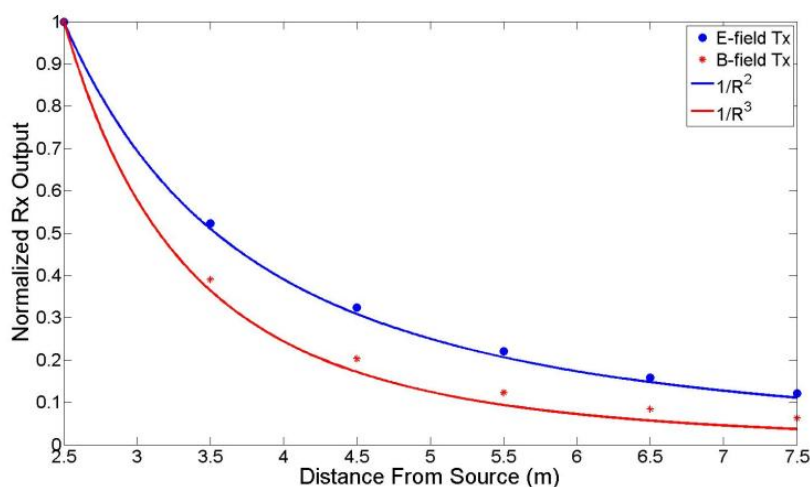


Figure 31. Normalized vertical magnetic field as measured with the wideband induction coil B field receiver with increasing range from the E or B field transmitters.

A limited set of data were acquired using the electric field receivers. In Figure 32 we show the time decay after the step off of a 4 ms square wave pulse due to a roughly 12 volt potential difference across the electrode transmitter. Long decays of over 50 ms are clearly seen above the background decays due to conduction currents. The longer target decay is mainly attributed to the induced polarization phenomena.

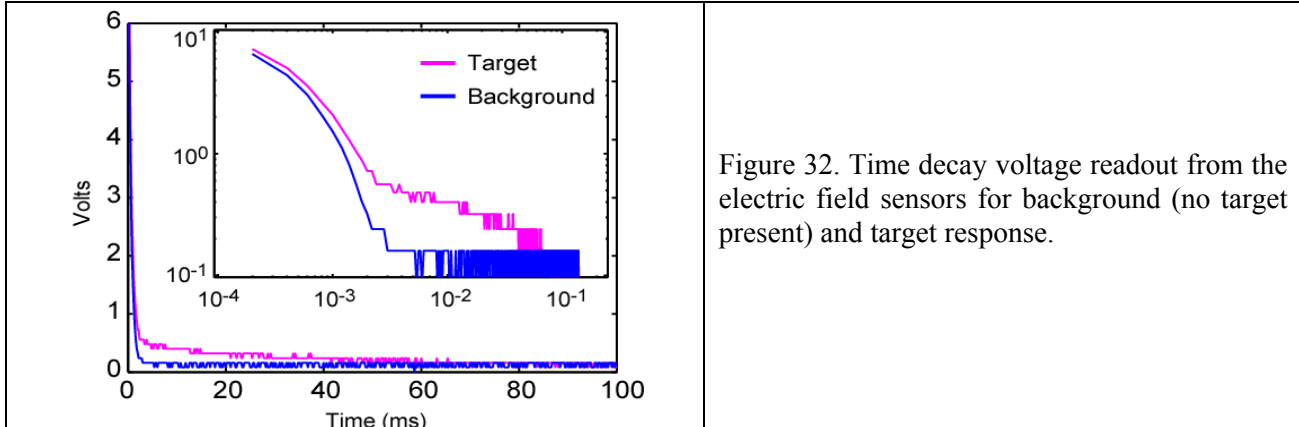


Figure 32. Time decay voltage readout from the electric field sensors for background (no target present) and target response.

By arranging the transmitter and receivers in nulled-coupled configurations we were able to essentially eliminate the primary field response from the transmitter. The induction coil transmitter (magnetic dipole) was arranged such that the vertical magnetic field, as recorded in the wideband induction coil B-field receiver, showed no variation while the transmitter output a 4ms square wave. Background measurements were made and compact metallic targets were placed at various positions and orientations relative to the transmitter and receiver. For the electric dipole transmitter we utilized the nulled vertical magnetic field perpendicular to the axis of the electrodes. Example raw voltage target decays (no filtering applied) are shown for the nulled magnetic field transmitter and electrode source in Figures 33.

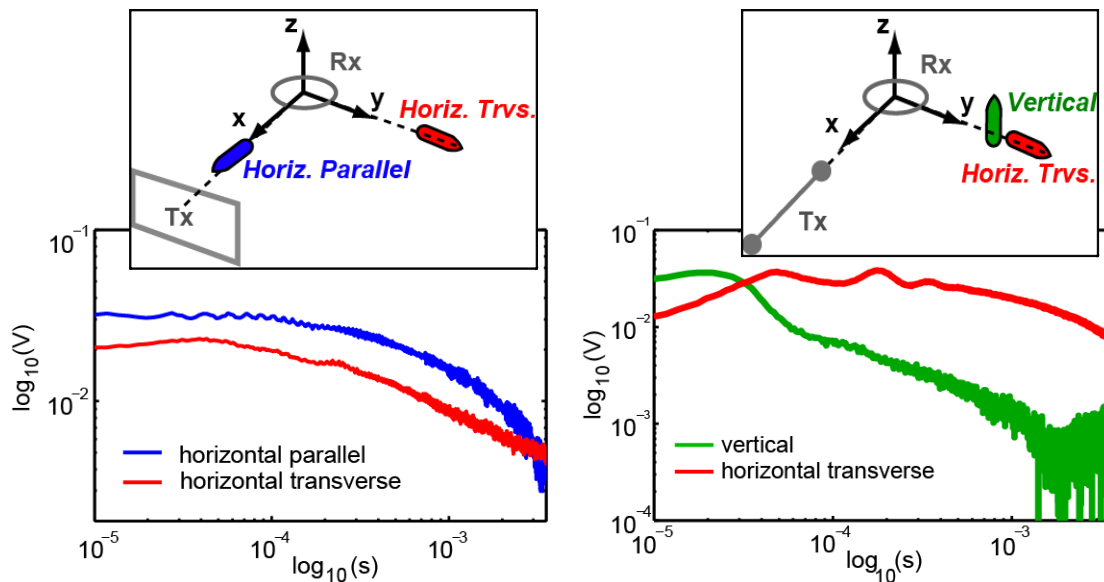


Figure 33. LEFT- Scattered B-field decay from a magnetic dipole transmitter. RIGHT Scattered B-field decay from a horizontal electric dipole.

With the magnetic dipole transmitter and B-field receiver in the nulled configuration we also acquired data with an “always on” source signal ranging from +12 VDC to -12 VDC at an 8 ms pulse repetition frequency. We acquired B-field receiver time decay data for various target types during both the ramp off and ramp on periods of the transmitter signal. Example target decays for ferrous and non-ferrous cylinders are shown in Figure 34.

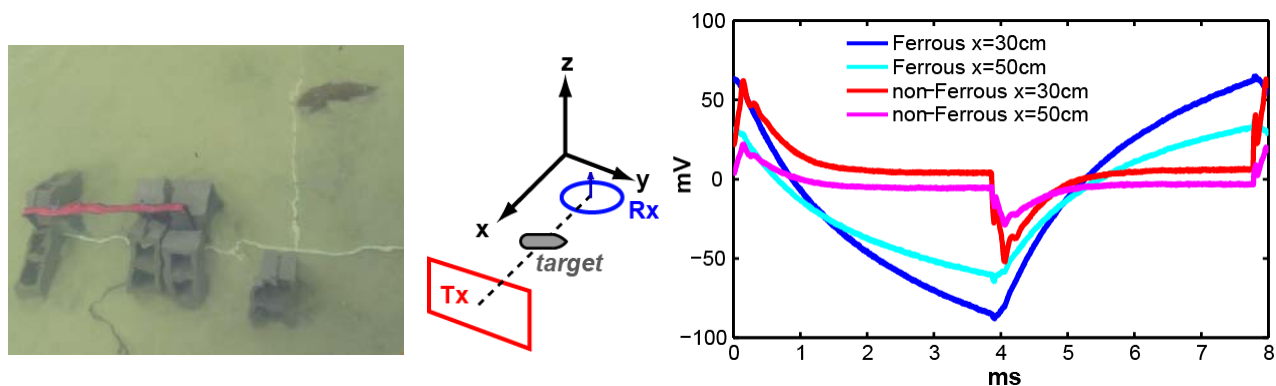


Figure 34. Scattered B-field response during ramp-off and ramp-on times for ferrous and non-ferrous targets.

### 2.3. Task 3 - Sensor Assessment and Concept Design Feasibility

Through execution of the aforementioned data collection and experimentation, we assessed the performance of several commercially available and custom sensors in facilitating collection of high quality data in the underwater environment. The insight gained through these experiments has provided us with an understanding of the concepts that best leverage the phenomenology associated with marine sites.

#### 2.3.1. Source Concepts

It is well known that electromagnetic waves attenuate much more rapidly in seawater than in air. Additionally, the high conductivity of seawater and the seafloor enables the formation of strong electrical currents that may exaggerate the ambient noise levels in conventional near-field EMI sensor data as a result of background response fluctuations. While the former condition precludes the use of high frequency terrestrial EM systems (e.g., GPR) and the latter condition complicates the deployment and degrades the performance of terrestrial EMI sensors (e.g., conventional induction coil systems), certain sensor deployment strategies will enable performance gains by exploiting specific elements of marine EM phenomenology. Most notable among these strategies are those that employ galvanic coupling with the environment.

As described in the Task 1 section, introducing an electric field source to the seawater environment will result in the flow of strong ionic conduction currents if the source electrodes are exposed to (i.e., galvanically coupled with) the water or seafloor. These conduction currents will flow not only directly between the electrodes, but also throughout the entire volume that the conductive medium fills. The associated current density is directly proportional to and follows the

electric field lines generated by the source. The result of this current distribution is a rotational magnetic field that decays more gradually with distance from the source than the magnetic field produced by a magnetic dipole source (i.e., those employed by conventional EMI sensors).

While the concept of galvanic coupling is certainly not limited to the marine environment (this practice has been well established by terrestrial IP surveys), the magnitude of the conduction currents is far greater in the marine environment than it is when associated with conduction currents produced by galvanic coupling of electrodes to soil. Furthermore, galvanic coupling is achieved with far greater ease in the marine environment than it is on land, thus making the process of acquiring soundings much more efficient and effective in seawater.

To demonstrate the improved range capability of the galvanic electric dipole source, we compared the magnetic field produced by our marine test coil (magnetic dipole source) to the magnetic field produced by our marine electrodes (electric dipole source). In order to quantify the range capability of each source, we evaluated the field strengths resulting when both systems drew the same amount of current (6 Amps nominal). We assessed the field strength versus range through modeling and direct measurement.

We used the previously described volume current density model to establish the field strength for the electric dipole source. In this case, we scaled the charge distribution on the electrodes to produce a total of 6 Amperes of current flow through each volume cross section passing between the electrodes. Similarly, we applied a Biot-Savart model to the magnetic dipole source coil carrying 6 Amperes of current. The resulting field strengths are plotted against range in Figure 35.

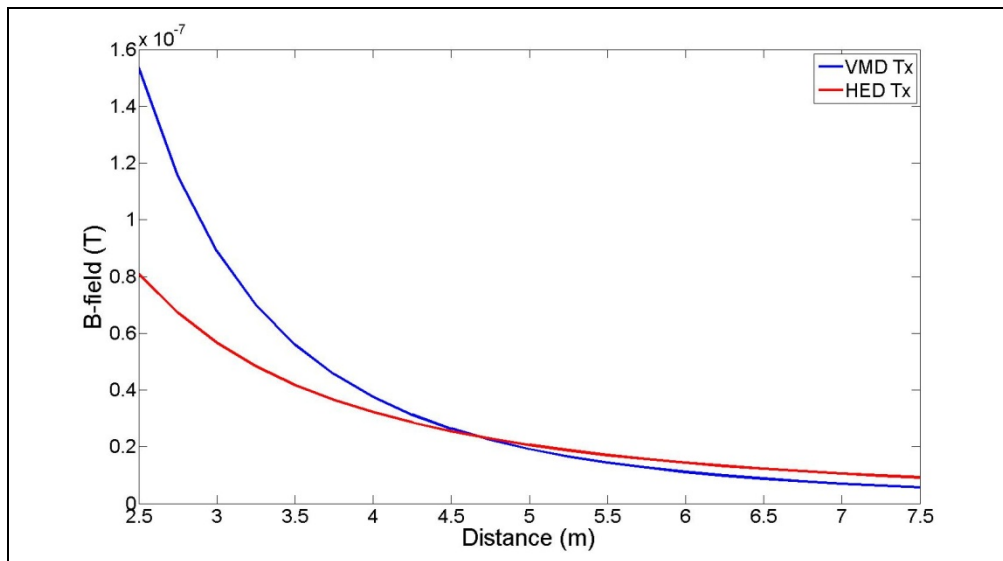


Figure 35. Rotational magnetic field intensity (red) calculated for horizontal electric dipole (HED) source and vertical magnetic field intensity (blue) calculated by vertical magnetic dipole (VMD) source plotted against distance from the source. Equal current draw is assumed for both sources. The rotational field decays more slowly than the vertical magnetic field.

During our open water tests, we performed a series of range experiments using the LEMI-134 wideband B-field sensor to measure the fields produced by each source. We also measured the current draw for each source and scaled the sensor output (measured in terms of A/D voltage) to

provide a direct comparison of the field strengths. Figure 36 shows the scaled measured field intensities compared to the modeled field intensities (all values are normalized to the E-field intensity).

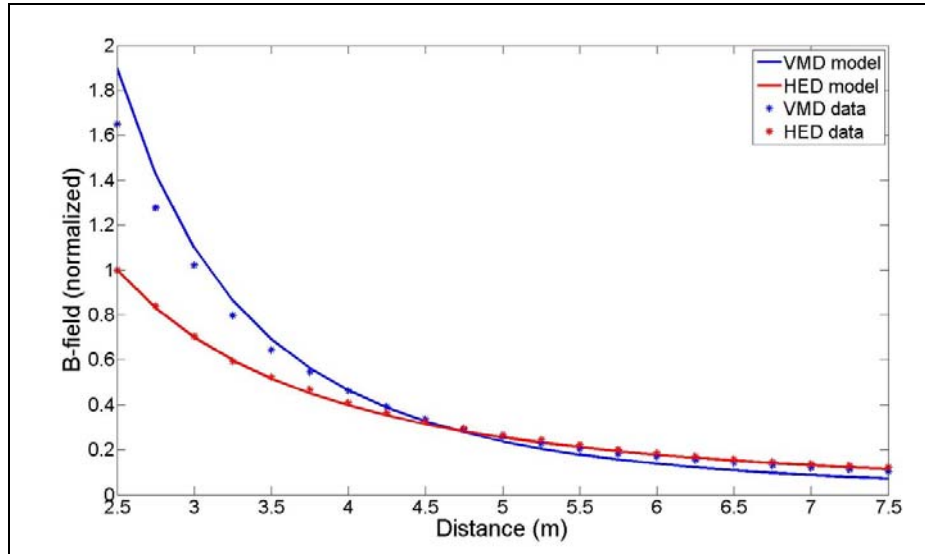


Figure 36. Calculated rotational and vertical magnetic field intensities (solid lines) compared to measured rotational and vertical magnetic field intensities (dots). Measurements confirm model predictions that indicate slower decay of rotational magnetic fields.

Both the model and the measurements indicate a crossover in the field intensity curves at a distance of approximately 4.5 m from the sources. After this point, the rotational magnetic field generated by the electric dipole is stronger than the magnetic field produced by the magnetic dipole source (given both sources are carrying equal current).

In addition to primary field range characterization, we also evaluated signal-to-noise ratio (SNR) of scattered fields induced by the two sources. For each source, we measured SNR for scattered fields generated by targets that were maximally coupled with the source. We used a vertically oriented 105mm target for the electrode source configured in a horizontal electric dipole (HED) orientation and we used a horizontally oriented 105mm target for the coil source configured in a horizontal magnetic dipole (HMD) orientation (Figure 37).

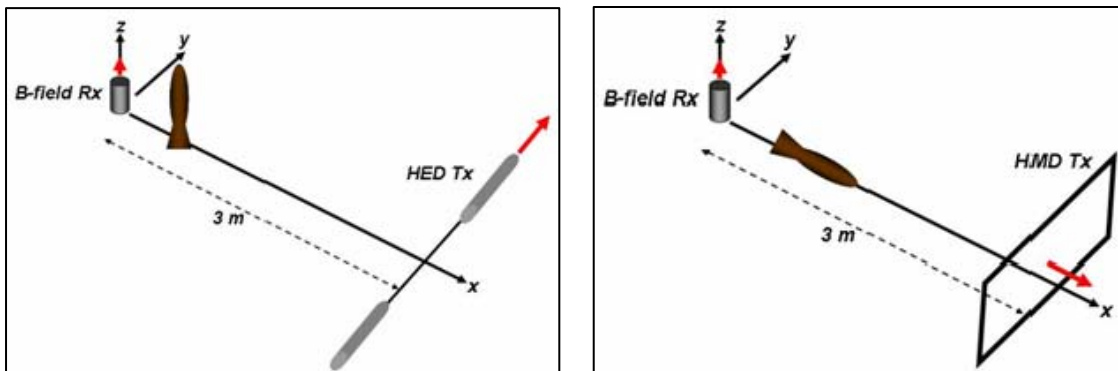


Figure 37. HED (left) and HMD (right) source/receiver configurations. Red arrows indicate direction of sensitivity for both sources and receivers. The HED source produces maximum magnetic field coupling when the target is z-oriented and the HMD source produces maximum magnetic field coupling when the

target is x-oriented. Measurements were obtained with the target positioned at different standoffs (along the x-axis) from the receiver.

Using the HED and HMD configurations, we isolated the scattered field generated by the target by subtracting the background response (i.e., no target present) from the total response (i.e., target present). We measured the scattered field magnitude for the target located at several offsets (x-directed) from the B-field receiver. SNR was determined by calculating the ratio of the peak-to-peak scattered field magnitude to the ambient noise standard deviation. For close ranges (50 cm), the HMD configuration provided a higher SNR (52 dB for the HMD compared to 48 dB for the HED); however, at greater target offsets (1 m), the HED configuration provided higher SNR (45 dB for the HED compared to 43 dB for the HMD). Figure 38 shows the measured scattered field response for each source with the target located at a 50 cm offset and at a 1 m offset.

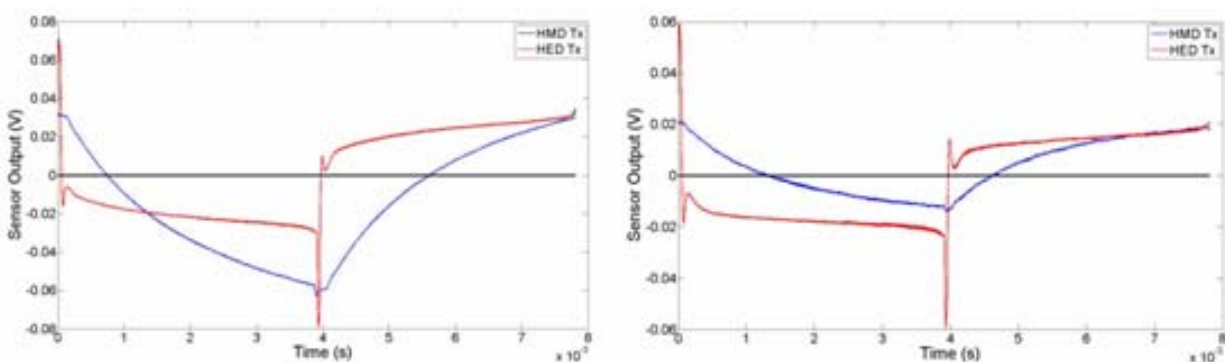
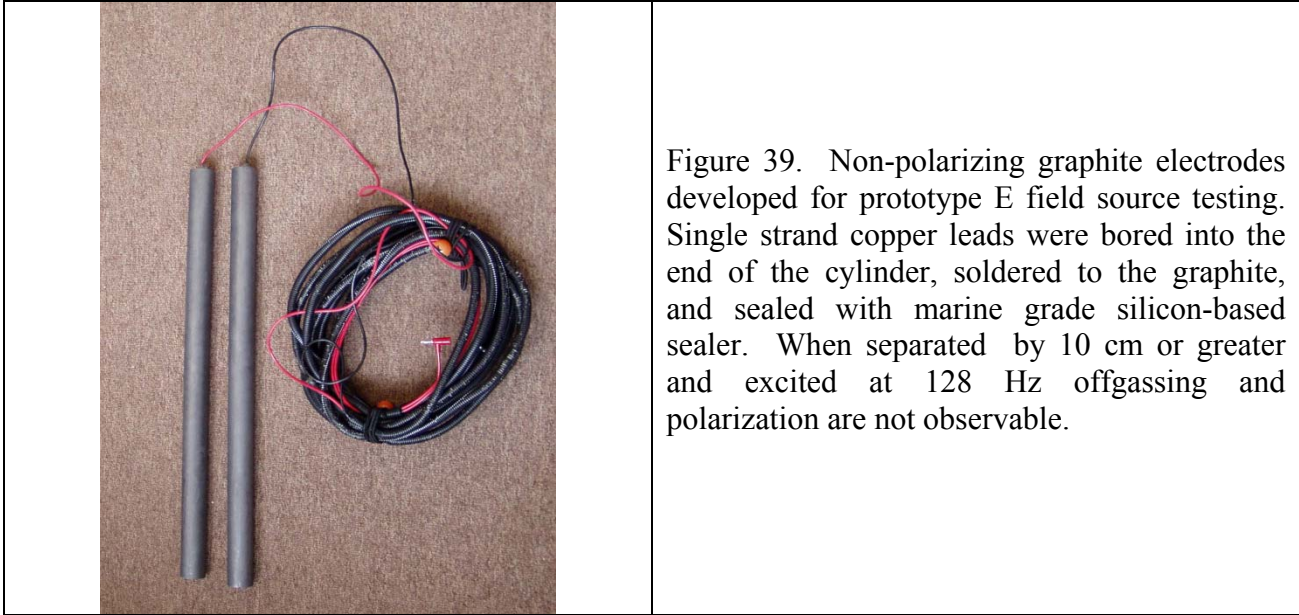


Figure 38. Scattered field measured in sensor voltage for the two configurations presented in Figure 37. At a 50 cm standoff (left) from the receiver, the target produces a stronger response when excited by the HMD source; however, at a 1 m standoff (right) the HED source elicits a stronger scattered field.

These data indicate that the HED source may provide better SNR for deeper targets. Ultimately, the benefit of employing a source capable of producing a rotational magnetic field (i.e., the HED source) will be the capability to generate a primary magnetic field that will remain stronger at greater ranges from the source than the field associated with a magnetic dipole transmitter. Additionally, for the given range capability, the rotational field transmitter will produce a slightly lower field strength at close ranges. This feature could be beneficial for reducing the primary field effect in the receivers when recovering signals from deep or distant targets.

### 2.3.2. Source Design

For our open water tests, we used a set of graphite electrodes (Figure 39). We selected a set of graphite rods similar to those used for heating electric arc steel furnaces. These electrodes are robust, easily machined, inexpensive, and are not influenced by the corrosion effects that rapidly deteriorate copper electrodes when used in seawater.



While we selected a pair of readily available industry standard graphite rods for the initial tests, we anticipate that a more refined selection process will be in place for a prototype source. Most importantly, we will identify design traits that minimize the contact resistance between the electrode and the seawater. These features will likely be a function of the electrode contact area (e.g., diameter, length, etc.). Additionally, we will determine the optimal configuration for the electrode spacing that maximizes current flow and dipole strength. For example, using our volume current density model, we can modify the electrode charge distributions to determine the maximum field output. Figure 40 shows the field strength versus range for the electrodes configured with varying separations (90 cm, 110 cm, and 130 cm) and driven with the same current level.

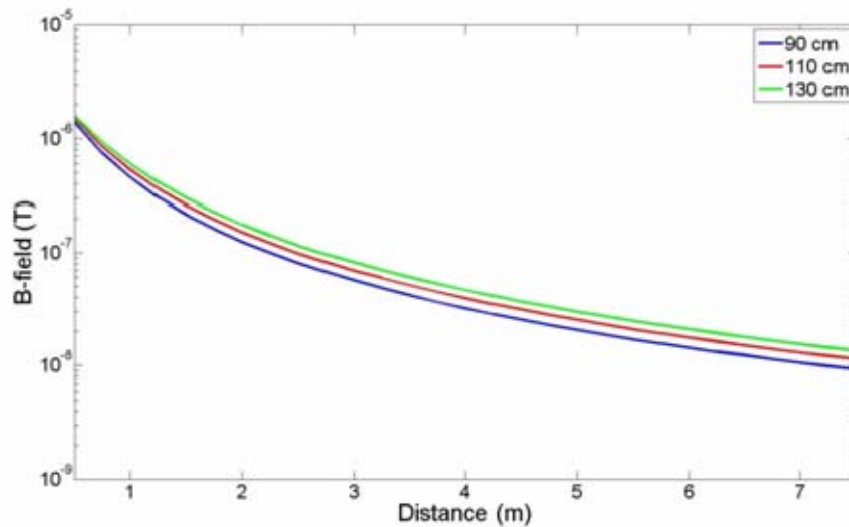


Figure 40. Modeled rotational field intensities for the HED source plotted against distance from the source. Each line corresponds to a specific electrode spacing. Assuming the electrodes draw the same current, greater separation produces a greater field strength.

Another challenge in the design of marine electric field sources is electrode polarization. Electrode polarization occurs because the dipole acts as a shunt across the field in the medium and electrons will flow into the dipole at one electrode and exit at another. In-addition to the electrons, negatively charged anions will be attracted to the anode and positively charged cations will be attracted to cathode. Given sufficient time, these ions form a cloud at the respective electrodes, thereby impeding the current flow through the dipole. As the frequency is increased, these clouds do not have time to form and therefore the impedance is smaller. In our experiments, we found that keeping the pulse repetition frequency above 128 Hz was sufficient for ensuring no ionic impedance resulted.

Multi-axis illumination can also be achieved with this source type, although further work is required to determine the best design. We advocate for the design of an electric field source with fast switching power transistors (e.g., MOSFET-based H-bridge circuit) to produce the bandwidth of interest (100 Hz to 200 kHz). Important design considerations will include electrode size and separation distance, drive voltage, and associated current. We have investigated preliminary concepts for a null driver and resistive load transfer to minimize the switching load based on conversations with marine hydrocarbon technology experts.

### **2.3.3. Receiver Concepts**

For nearly all underwater/marine electromagnetic sensing modalities (e.g., DC resistivity, induced polarization, electromagnetic induction, radar), the electric and magnetic fields are greatly reduced over the values that would be encountered in similar land-based surveys. The conductive water, which is responsible for the decreased electromagnetic field amplitudes, also produces some advantages – namely that measurement of smaller signals is possible if correct advantage is taken of the underwater environment (Evans, 2001). For near-field AC electric field sensing (as opposed to DC resistivity or induced polarization), noise is reduced throughout the spectrum because low impedance contact with freshwater or seawater is easily established and the water column provides thermal and chemical stability relative to that on land. The underwater environment also has a smoothing effect on electric fields (Chave et al., 1991) because the great electrical thickness of the water column and relatively high conductivity dominate the effects of small-scale heterogeneities in the sea-bottom (i.e., geologic noise).

Wideband B-field, wideband E-field, and induction coil (dB/dt) sensors are all feasible options for receivers that could be paired with an electric dipole source. We conducted our tests with passive wideband E- and B-field sensors as these account for both static and dynamic phenomenology, in contrast to induction coil receivers, which account only for transient effects. We collected data and performed modeling for receivers in both the broadside and in-line configurations, as shown in Figure 41.

During selection of prototype receivers, consideration should be given to inherent noise capabilities. Given a comparison of E- and B-field sensors that offer similar noise characteristics, the wideband B-field sensor may be the optimal receiver choice as it will fully leverage the rotational magnetic field range attributes. Our initial tests with the commercial receivers we selected for the open water experiments indicated comparable noise performance for both the E-field and B-field sensors.

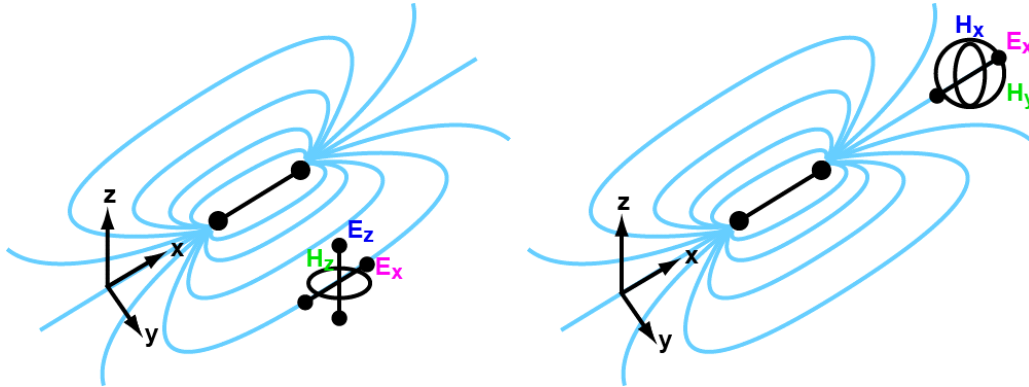


Figure 41. For the broadside configuration (left), the z-directed magnetic dipole receiver is maximally coupled with the electric dipole source. For the in-line configuration (right), the source field is nulled with respect to the magnetic field receivers.

For our experiments we utilized compact 3-axis electrochemical cell-type electrodes for sensing electric fields at the nanoVolt level. Electrochemical cell electrodes were chosen over nonpolarizing metal electrodes (such as zinc or graphite as are sometimes used on land) because of their superior sensitivity, impedance matching, and resistance to polarizing in sea water. The Ag/AgCl electrode configuration has been found to have the best performance in saltwater. A dipole pair are used for measuring a voltage potential difference, which can be easily related the electric field intensity. We tested two commercial versions of compact sensors (from Information Systems Laboratory and Ultra Electronics PMES). Only slight variations were noted between the designs and performance.

One challenge in the fabrication of Ag/AgCl electrodes (aside from their intrinsic noise) is their potential to produce spurious signals if temperature or salinity change abruptly (Filoux, 1978). This is greatly reduced by the use of a Ag electrodes embedded in gelatin-based solutes in place of electrodes potted directly in a liquid AgCl solution separated from the sea by a permeable membrane. The basic design for the electrodes we used following this technique and is shown in Figure 42.

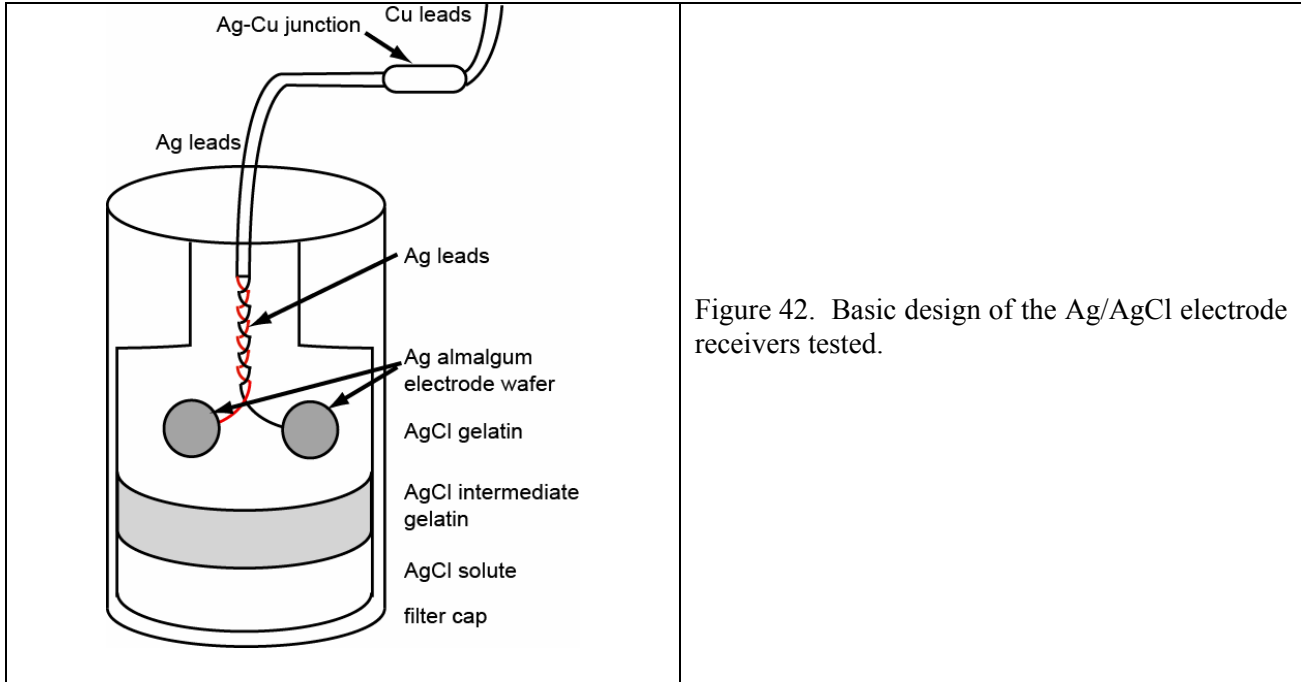


Figure 42. Basic design of the Ag/AgCl electrode receivers tested.

Another challenge in the design of the marine electric field sensors is electrode polarization. Electrode polarization occurs because the dipole acts as a shunt across the field in the medium and electrons will flow into the dipole at one electrode and exit at another. In-addition to the electrons, negatively charged anions will be attracted to the anode and positively charged cations will be attracted to cathode. Given sufficient time, these ions form a cloud at the respective electrodes, thereby impeding the current flow through the dipole. As the frequency is increased, these clouds do not have time to form and therefore the impedance is smaller.

### 2.3.4. Receiver Design

We evaluated a number of receiver configurations to maximize the scattered field response from a number of targets. While not a required feature, configurations that result in a cancellation of the primary field at the receiver location may provide the added benefit of enabling on-time (during the transmitter-on period) measurements. We evaluated several of these “nulled” configurations and found the scattered field measurements to be quite strong during both on- and off-time portions of the transmit cycle without performing any background subtraction. Figure 43 shows an in-line electric dipole source/B-field receiver combination that presents a solution for on- and off-time sensing in a robust package that could be towed in a streamer configuration along the seafloor.

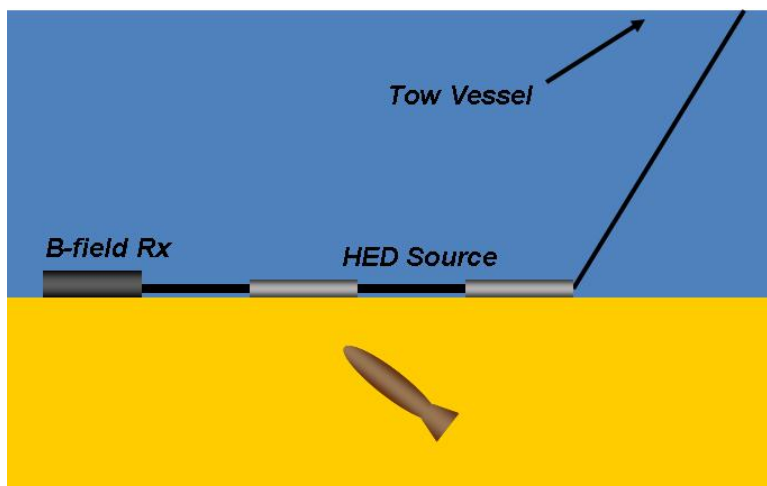


Figure 43. Conceptual illustration of an in-line source/receiver configuration. The HED source generates a rotational magnetic field that excites buried objects. The field scattered by the target is measured in the horizontally directed B-field receiver. The primary field from the source is cancelled in the receiver to enable full waveform measurements of the scattered field.

### 3. Year 2 Suggested Work

The primary objective for Year 2 is to develop a working prototype for an active E-field source/B-field receiver system. The associated efforts will include physical modeling to optimize the design of the source/receiver configuration, procurement and fabrication of parts and equipment to assemble the prototype system, and field testing of the system from a tow vessel. Details of these efforts are as follows:

#### **Task 1. Focused Modeling and Simulation of E-field Source / B-field Receive System.**

We will apply the models developed under the Year 1 modeling task specifically for optimizing the source/receiver configuration design. We will examine factors such as electrode spacing, electrode geometry, seafloor standoff sensitivity, source/receiver separation, and source/receiver orientation to guide selection of optimal design features. Additionally, we will use spectral analysis to determine the requirements for transmitter waveform, receiver bandwidth, and data acquisition sampling rates.

Finally, we will use the models as a guide for assessing the merits of employing E-field receivers in addition to the B-field receiver. While the data collection and modeling to date indicate that the wideband B-field sensor accounts for all aspects of the marine EM phenomenology that we are interested in examining, there may be additional benefits to including the E-field receiver as well. We will apply the models to determine the value of such a design if deemed practical.

#### **Task 2. Hardware Component Design and Development.**

Prior to final design and component selection, we will perform additional testing of candidate sensors. Primarily, this effort will focus on evaluating the feasibility of deploying E-field receivers in addition to the wideband B-field receiver. If modeling results indicate a significant gain would be realized by employing the E-field sensors, we will identify the hardware requirements for integrating these receivers with a towed system.

Because galvanic coupling from an electric dipole source was found to generate strong and widely distributed primary field conduction currents that fall off as  $1/r^2$ , we think that a carefully designed E-field transmitter will generate adequate excitation of targets at standoff distances up to 3 meters. Therefore, we will develop and trial an electric dipole source based on lessons learned from our previous experimental system. To accomplish this, we will extend and test a configurable source input design that enables wideband excitation fields with goal of achieving 200 kHz bandwidth. Coupled with potential for improved form factor and reduced hydrodynamic drag, we contend that this source may ultimately outperform an induction coil transmitter as a source when cost effectiveness, ease of deployment, and source strength at range are considered. Multi-axis illumination can also be achieved with this source type, although further work is required to determine the best design.

Additionally, we will conduct limited testing of the E-field source/B-field receiver configuration to determine optimal deployment strategies. For example, we will evaluate the necessity for rigidly coupling the source to the receiver as well as the requirement for producing a nulled configuration (i.e., no primary field response measured by the receiver). We will also consider solutions for enabling positioning of the prototype system (e.g., encoder-based kinematic positioning) when deployed from a tow vessel. These requirements will be determined through a series of laboratory and controlled (near site) field tests.

The process of acquiring additional data will also provide an opportunity to fine tune data acquisition parameters. We will develop a data acquisition system, including software control module, to facilitate integrated sensor data acquisition and processing. Specifically, we will establish the hardware requirements for producing a data acquisition unit that will be integrated with the prototype system.

### **Task 3. Towed Prototype Fabrication and Testing.**

Following optimal design and sensor selection, we will fabricate a prototype system capable of deployment from a tow vessel. This task will include procurement of commercial components, fabrication of custom components, and assembly of the sensing unit, positioning/tow unit, and the data acquisition unit. The major challenge associated with this effort will be ensuring all components are sufficiently protected from ingress of water, which may necessitate fabrication and assembly of pressure vessels for certain components. An additional challenge will be providing rigid coupling between the source and receiver if a nulled configuration is desired. We anticipate this design can be achieved by applying a marine epoxy during the fabrication process.

Upon completion of the prototype fabrication, we will test the system at an underwater site using a tow vessel to deploy the sensors. This effort will serve as a validation of the technology as well as the approach. We anticipate deploying the sensor in relatively shallow water (2-20m) for this test as this will facilitate placement of targets as well as ground truthing. Data collected will be analyzed for range sensitivity, SNR, and target characterization, as well as the advantages and limitations of various deployment strategies.

## REFERENCES

- Bannister, P.R., 1984, New simplified formulas for ELF subsurface-to-subsurface propagation, *IEEE Jour. Ocean Engineering*, OE-9, 154-163.
- Born, M. and E. Wolf, 1999, *Principles of Optics*, University Press, Cambridge, 7th edition.
- Chave, A.D., and C.S. Cox, 1982, Controlled source electromagnetic sources for measuring electrical conductivity beneath oceans, 1. Forward problem and model study, *Journal of Geophysical Research*, 87, 5327-5338.
- Chave, A.D., Constable, S.C., and R.N. Edwards, 1986, Electrical exploration methods for the seafloor: In Nabighian, M.N., Ed., *Electromagnetic Methods in Applied Geophysics*, Vol. 2: Applications, Soc. Expl. Geophys., Tulsa.
- Chave, A.D., 2009, On the electromagnetic fields produced by marine frequency domain controlled sources, submitted to *Geophysical Journal International*.
- Cheesman, S. J., Edwards, R. N., Chave, A. D., 1987. On the theory of sea-floor conductivity mapping using transient electromagnetic systems. *Geophysics*, 52, 204 -217.
- Constable, S. and C. Cox, 1996, Marine controlled source electromagnetic sounding – II: The PEGASUS experiment, *Journal of Geophysical Research*, 97, 5519-5530.
- Dey, A., S. Ward, 1970, Inductive sounding of a layered earth with a horizontal magnetic dipole, *Geophys*, 35, 660-703.
- Evans, R.L. and M. E. Everett, 1994, Discrimination of hydrothermal mound structures using transient EM methods, *Geophys. Res. Letts.*, 21, 501-504.
- Evans, R.L., 2001, Measuring the shallow porosity structure of sediments on the continental shelf: A comparison of an electromagnetic approach with cores and acoustic backscatter, *J. Geophys. Res.*, 106 (C11), 27047-27060.
- Evans, R.L., 2007, Using controlled source electromagnetic techniques to map the shallow section of seafloor: From the coastline to the edges of the continental slope, *Geophysics*, 72, 105-116.
- King, R.W.P., 1989, Lateral electromagnetic waves from a horizontal antenna for remote sensing in the ocean, *IEEE Trans. Antennas and Propagation*, 37, 1250-1255.
- Loseth, L.O., 2007, Modeling of controlled source electromagnetic data, PhD Thesis, Norwegian University of Science and Technology, Department of Physics, 176 pp.
- MacGregor, L.M., Sinha, M.C., and S.C. Constable, 2001, Electrical resistivity structure of the Valu Fa Ridge, Lau basin, from marine controlled source electromagnetic sounding, *Geophys. Jour. International*, 146, 217-236.
- SERDP, 2007, SERDP&ESTCP Workshop on Technology Needs for the Characterization, Management, and Remediation of Military Munitions in Underwater Environments, 45 pp.
- Shubitidze, F., Shamatava, I., Fernandex, J.P., and B. Barrowes, 2009, MM-1632 Modeling EMI scattering phenomena in a conducting environment to enhance underwater UXO detection and discrimination, *Proc. of the SERDP & ESTCP Partners Symposium*, Washington DC.
- Straton, J.A., 1941, *Electromagnetic Theory*, McGraw-Hill, New York, 615 pp.
- Wait, J. R., 1962, *Electromagnetic Waves in Stratified Media*. Pergamon Press, Oxford
- Wait, J.R., 1995, Excitation of a conducting half-space by a toroidal coil, *IEEE Antennas and Propagation*, 37, 72 – 74
- Wait, J.R., “Electromagnetic field of current carrying wires in a conducting medium,” *Canadian Jour. Physics*, 30(5), 512-523, 1952.
- Wait, J.R., Campbell, L.L., “The fields of an oscillating magnetic dipole immersed in a semi-infinite conducting medium,” *Jour. Geophysical Research*, 58(2), 167-178, 1953.